| | |
|---|---|
| **Titre:** Title: | Characterization of an Offset-Stabilized Dual-Frequency Comb System at 1.55 µm Toward Broadband Absorption Spectroscopy |
| **Auteur:** Author: | Émile Dessureault |
| **Date:** | 2024 |
| **Type:** | Mémoire ou thèse / Dissertation or Thesis |
| **Référence:** Citation: | Dessureault, É. (2024). Characterization of an Offset-Stabilized Dual-Frequency Comb System at 1.55 µm Toward Broadband Absorption Spectroscopy [Mémoire de maîtrise, Polytechnique Montréal]. PolyPublie. https://publications.polymtl.ca/58340/ |



| | |
|---|---|
| **URL de PolyPublie:** PolyPublie URL: | https://publications.polymtl.ca/58340/ |
| **Directeurs de recherche:** Advisors: | Denis Seletskiy, & Frédéric Lesage |
| **Programme:** Program: | Génie physique |

**POLYTECHNIQUE MONTRÉAL**
affiliée à l'Université de Montréal

# Characterization of an Offset-Stabilized Dual-Frequency Comb System at 1.55 µm Toward Broadband Absorption Spectroscopy

**ÉMILE DESSUREAULT**
Département de génie physique

Mémoire présenté en vue de l'obtention du diplôme de *Maîtrise ès sciences appliquées*
Génie physique

Mai 2024

**POLYTECHNIQUE MONTRÉAL**
affiliée à l'Université de Montréal

Ce mémoire intitulé :

**Characterization of an Offset-Stabilized Dual-Frequency Comb System at 1.55 µm Toward Broadband Absorption Spectroscopy**

présenté par **Émile DESSUREAULT**
en vue de l'obtention du diplôme de *Maîtrise ès sciences appliquées*
a été dûment accepté par le jury d'examen constitué de :

**Sébastien FRANCOEUR**, président
**Denis SELETSKIY**, membre et directeur de recherche
**Frédéric LESAGE**, membre et codirecteur de recherche
**Juan Nicolás QUESADA MEJIA**, membre

## DEDICATION

*To the ones who believed in me*

## ACKNOWLEDGEMENTS

I want to deeply thank my research director Prof. Denis Seletskiy for the opportunity to work in a stimulating state-of-the-art laboratory. He guided and encouraged me throughout the entirety of my master's project and it would never have been possible without his support. I also thank Dr. Stephane Virally who helped to manage our research group and always tried to push my understanding of my project to a deeper level.

I want to thank my codirector Prof. Frédéric Lesage who always found a way to motivate me. I particularly appreciate his support and the place he made for me in his lab. I'd like to thank Patrick D.-M. for the daily help in the lab and for the enlightening discussions we had.

I thank all my friends and colleagues Gabriel, Patrick C., Grégory-Samuel, Justine, Amin, Laurent, Marco, Étienne, Sho, Shilong that are or have been in the femtoQ group during my master's. I especially want to thank Gabriel who has been a great mentor when I joined the group, for the tremendous help and support he gave me in the past three years and making the group a fun place to work in. I could not be more grateful to Pat for the numerous technical and friendly discussions. Thank you Laurent for the help with the FROG setup and for the pyNLO simulations.

I want to thank my parents Fabien and Marie-Josée and siblings Mathilde and Félix who never stopped believing in me during this adventure, it really means a lot. Thank you so much Émilie for being by my side and for the support during the hardest times.

# RÉSUMÉ

La portion infrarouge du spectre électromagnétique contient plusieurs résonances fondamentales telles que les modes ro-vibrationnels de gaz ou de molécules organiques et leur caractérisation ainsi que leur identification sont possibles à partir de la spectroscopie d'absorption. Traditionnellement, les mesures à large bande spectrale se font avec un interféromètre de Michelson ayant des composantes mobiles qui appliquent un délai variable sur une branche de l'interféromètre. Dans le but d'améliorer la résolution, l'exactitude, la sensibilité ou le temps d'acquisition des mesures spectroscopiques d'échantillon gazeux, une nouvelle technique de spectroscopie à double-peignes fréquentiels a été développée au cours des deux dernières décennies. Cette méthode consiste à interférer deux lasers stabilisés à verrouillage de modes ayant des taux de répétition légèrement différents et génère un signal composé d'interférogrammes périodiques contenant la signature spectrale de l'échantillon, et ce sans aucune pièce mobile. Comme le contenu spectral de chaque interférogramme est identique, ils peuvent être moyennés de façon cohérente pour augmenter le signal-sur-bruit, et donc la sensibilité. Typiquement, les sources de lumière utilisées avec les interféromètres de Michelson sont des lampes thermiques ayant des statistiques sur-Poissonienne, tandis que les lasers, avec des statistiques Poissonienne, permettent des mesures limitées par le *shot-noise*. La résolution spectrale est maintenant déterminée par l'espacement entre les composantes spectrales des peignes fréquentiels plutôt que par le délai maximal qu'un interféromètre de Michelson peut appliquer.

Ainsi, un interféromètre à double-peignes fréquentiels ayant une différence de taux de répétition stabilisée et une longueur d'onde centrale à 1.55 $\mu$m est assemblé et caractérisé pour permettre des mesures spectroscopiques précises, à large bande spectrale et à haut signal-sur-bruit. Deux peignes de fréquences commerciaux avec un taux de répétition nominal $f_{rep}$ =100 MHz ainsi qu'une différence de taux de répétition ajustable et stabilisée de quelques kHz sont interféré pour produire un peigne de fréquences radio ayant des composantes espacées par $\delta f_{rep}$. Les interférogrammes y correspondant sont séparés par $1/\delta f_{rep}$ et sont mesurés dans le domaine temporel par un détecteur lent. Notre système est composé de deux peignes en opération libre et leur cohérence mutuelle est maintenue par une boucle à verrouillage de phase qui stabilise leur différence de taux de répétition, tandis que la *carrier-envelope offset frequency* $f_{ceo}$ pour chaque peigne n'est pas stabilisée.

Les peignes fréquentiels sont caractérisés avec un montage de *second-harmonic generation frequency-resolved optical gating* (SHG-FROG), puis la stabilité dans le temps de leurs taux

de répétition et $f_{ceo}$ est évaluée. Un montage optique expérimental se basant sur le mélange d'états de polarisation pour interférer les deux peignes est assemblé pour mesurer le spectre optique de la source à deux peignes. Une procédure pour moyenner les interférogrammes séquentiels de façon cohérente à partir d'interpolations et d'un ré-échantillonnage du signal est implantée et révèle un temps de cohérence effectif entre les peignes de l'ordre de 40 ms. Des assemblages de fibres hautement nonlinéaires sont conçus pour élargir le spectre optique de chaque laser avant de les combiner pour chevaucher davantage le spectre d'absorption dans l'infrarouge proche d'un échantillon acétylène. Une comparaison entre une mesure préliminaire réalisée avec notre système à deux peignes et la base de données HITRAN pour ce même échantillon montre un accord qualitatif, ce qui constitue une avancée vers des mesures spectroscopiques à large bande.

# ABSTRACT

The infrared region of the electromagnetic spectrum is home to many fundamental resonances such as ro-vibrational modes of gases or organic molecules and their characterization and identification can be done via absorption spectroscopy. Traditionally, broadband measurements are done with auto or cross-correlation techniques by means of a mechanically scanned Michelson interferometer. Aiming to improve the resolution, accuracy, sensitivity or acquisition time of spectroscopic measurements of optically active gaseous samples, a new dual-frequency comb spectroscopy technique has been developed in the past two decades. Relying on the interference of two stabilized mode-locked lasers with slightly different repetition rates, a cross-correlation signal made of periodic interferograms containing the signature of the sample is generated without any moving parts. Containing the same spectral information, the sequential interferograms can be coherently averaged to increase the signal-to-noise and thus the sensitivity. Traditional Fourier-transform infrared spectroscopy typically uses thermal light, which has super-Poissonian statistics, while laser light, with Poissonian statistics, intrinsically operates at the shot-noise level, thus directly improving the signal-to-noise characteristics of the measurement. The spectral resolution is now set by the frequency-domain tooth spacing of the frequency combs rather than by the finite travel range of Michelson interferometers.

With those advantages in mind, an offset-stabilized dual-frequency comb interferometer with a central wavelength of 1.55 $\mu$m is assembled and characterized aiming to perform fast, precise, broadband and high signal-to-noise optical spectroscopy. Two commercial frequency combs with nominal repetition rates $f_{rep}$=100 MHz and tunable stabilized repetition rate difference $\delta f_{rep}$ of few kHz are interfered to produce a radio-frequency comb with $\delta f_{rep}$ mode spacing, where the corresponding interferograms occurring every $1/\delta f_{rep}$ are measured in the time domain with a low-bandwidth detector. Our system is composed of two free-running frequency combs that are made mutually coherent via a phase-locked-loop ensuring a stable repetition rate difference in time while their carrier-envelope offset frequency $f_{ceo}$ is left unstabilized.

The characterization steps of the individual combs include second-harmonic generation-frequency-resolved optical gating and time-stability measurements of their $f_{ceo}$ and $f_{rep}$ parameters. An optical setup to interfere the repetition rate-detuned combs based on polarization mixing is assembled and used to measure the optical spectrum of the dual-frequency comb source. A procedure to coherently average the sequential interferograms relying on

post-measurement numerical interpolation and resampling is implemented to reveal an effective coherence time on the order of 40 ms. Home-made assemblies of highly nonlinear fibers are designed to broaden the optical spectrum of both combs prior to their combination to better overlap with the near-infrared absorption features of an acetylene sample. A comparison between a preliminary measurement made with our dual-frequency comb system with the HITRAN database for acetylene shows qualitative agreement which is a step closer toward broadband spectroscopy.

# TABLE OF CONTENTS

# LIST OF FIGURES

# LIST OF SYMBOLS AND ACRONYMS

| | |
|---|---|
| IR | Infrared |
| NIR | Near Infrared |
| MIR | Mid Infrared |
| FTIR | Fourier-Transform Infrared |
| FFT | Fast Fourier-Transform |
| IGM | Interferogram |
| SNR | Signal-to-Noise Ratio |
| CW | Continuous-Wave |
| DFC | Dual-Frequency Comb |
| RF | Radio-Frequency |
| PLL | Phase-Locked Loop |
| HITRAN | High-Resolution Transmission |
| HNF | Highly Nonlinear Fiber |
| SESAM | Semiconductor Saturable Absorber Mirror |
| FWHM | Full-Width Half-Max |
| FTL | Fourier-Transform Limit |
| GD | Group Delay |
| GDD | Group Delay Dispersion |
| TOD | Third Order Dispersion |
| FROG | Frequency-Resolved Optical Gating |
| SHG | Second-Harmonic Generation |
| SFG | Sum-Frequency Generation |
| BS | Beam-Splitter |
| CEO | Carrier-Envelope Offset |
| CEP | Carrier-Envelope Phase |
| EOM | Electro-Optic Modulator |
| AOM | Acousto-Optic Modulator |
| PZT | Piezoelectric Transducer |
| DFG | Difference-Frequency Generation |
| SCG | Supercontinuum Generation |
| HHG | High-Harmonic Generation |
| VIPA | Virtually Imaged Phased Array |
| OSA | Optical Spectrum Analyzers |

| | |
|---|---|
| DC | Direct Current |
| ADC | Analog-to-Digital Converter |
| PFID | Perturbed Free Induction Decay |
| HWP | Half-Wave Plate |
| BBO | Beta Barium Borate |
| COPRA | Common Pulse Retrieval Algorithm |
| COSMO | Comb Offset Stabilization Module |
| PI | Proportional-Integral |
| BD | Balanced Detection |
| ND | Neutral Density |
| PBS | Polarizing Beam-Splitter |
| WP | Wollaston Prism |
| CMRR | Common-Mode Rejection Ratio |
| SPM | Self-Phase Modulation |
| RK4IP | Fourth-order Runge-Kutta in the Interaction Picture |
| PPLN | Periodically Poled Lithium Niobate |

# LIST OF APPENDICES

# CHAPTER 1 INTRODUCTION

## 1.1 General Introduction

In the context of optics, spectroscopy is the field that studies the frequency dependence of light-matter interactions by analyzing the absorption and emission spectrum of a sample [6]. Every analyte has its own signature, and spectroscopy can be used to reveal the nature of an unknown sample. To do so, only a light source and detector are needed. Two measurements are required for absorption, one with the sample placed between both the source and detector and another without. Each measurement produces a frequency spectrum and a comparison between both yields the absorption spectrum of the sample. Spectroscopy is useful in a variety of fields for many applications, ranging from greenhouse gas monitoring [7, 8] to non-invasive breath analysis [9] and quality control of food and pharmaceuticals [10, 11] to name a few.

There are many gases whose constituents have rotational and vibrational modes that are active at frequencies corresponding to the infrared (IR). Specifically, both the near and mid-infrared (NIR, MIR) regions (wavelengths of 0.78-2.5 $\mu$m and 2.5-50 $\mu$m, respectively) are home to many rovibrational modes of organic molecules. This so-called molecular fingerprint region of the electromagnetic spectrum is thus ideal to perform spectroscopy [12], but is also challenging because of the general lack of sources and detectors.

Among the IR sources, black-body radiation sources such as thermal lamps and globars have been and still are widely used to perform broadband spectroscopy. They enabled simple absorption spectroscopy and were eventually combined with what is now known as the Michelson-Morley interferometer. Although it was not initially designed for this purpose [13], this new tool enabled Fourier-Transform Infrared (FTIR) spectroscopy by interfering two delayed copies of the same light source and can be considered as an auto-correlator in the time domain. The corresponding frequency-domain information is revealed by a Fast Fourier Transform (FFT) of the time-domain signal known as an interferogram (IGM). Even if their instrumental line-shape is well understood and modelled accurately, the FTIR technique has multiple inherent drawbacks. The delay is applied by a mechanical stage that is prone to external vibrations and travels at a relatively slow speed. This results in important dead times between each stage position such that a total measurement generally takes on the order of seconds to minutes. The spectral resolution of these interferometers is set by the maximal travel range of the moving stage such that high-resolution scans require few-meter path delays, where spatial mode-matching becomes challenging to maintain and affects the

visibility (or contrast between destructive and constructive interference) and thus the sensitivity. Also, traditional sources used in FTIR present super-Poissonian statistics which limits the best attainable Signal-to-Noise Ratio (SNR) [14].

Advances in ultrafast photonics from the past few decades made it clear that pulsed lasers relying on mode-locking could provide a solution that could solve the challenges mentioned above. Being made of several and equally spaced-out longitudinal modes, the spectrum of a mode-locked laser can be seen as an array of phase-locked Continuous-Wave (CW) lasers that effectively forms a *frequency comb*. This new sub-class of coherent sources benefit from Poissonian statistics and enable shot-noise limited measurements. In fact, frequency combs turned out to be one of the subjects of the 2005 physics Nobel prize awarded to Roy J. Glauber, John L. Hall and Theodor W. Hänsch.

Aiming to solve the technical issues encountered with FTIR spectrometers, a relatively new Dual-Frequency Comb (DFC) spectroscopy technique emerged about 20 years ago. As it may be deduced from its name, this method relies on the interference of two frequency combs with slightly different repetition rates $f_{rep}$ and $f_{rep}+\delta f_{rep}$ that generate a repetitive cross-correlation signal at a frequency corresponding to the repetition rate difference $\delta f_{rep}$. The repetition rate of frequency combs is commonly on the order of a couple MHz to a couple GHz and the detuning $\delta f_{rep}$ between a couple Hz to few tens of kHz, which means a new DFC IGM is produced in under a couple microseconds to milliseconds. In the frequency domain, the longitudinal modes of each comb interfere to generate a multi-heterodyne beat signal forming a radio-frequency (RF) comb with a mode spacing of $\delta f_{rep}$, which requires a slow detector instead of resolving optical frequencies. The sequential IGMs contain the same spectral information and can thus be averaged to improve the SNR. The spectral resolution in DFC measurements is now set by the repetition rate of the combs since all of their longitudinal modes act as spectral sampling points. Some DFC systems are very compact (shoe-box sized) and now even smaller as on-chip DFC interferometers have been reported [15].

## 1.2 Research Objectives

As it was a first attempt for our research group to employ a DFC system, with the aim of upgrading it in a separate study, the main objective was to familiarize ourselves with DFC measurements and the theoretical aspects behind them. The scope of this research project was to characterize a proof-of-principle repetition rate offset-stabilized DFC setup using two commercially available frequency combs at 1.55 $\mu$m. This is done via the assembling and characterization of the Phase-Locked Loop (PLL) locking both combs together and the free-space optical setup enabling spectroscopic measurements of samples. Furthermore, we wanted

to quantify the coherence time of our DFC system by coherently averaging sequential post-processed IGMs. The performances of the characterized setup are tested by comparing our experimental absorption measurements of an acetylene sample against the ones from the high-resolution transmission (HITRAN) molecular absorption database.

### 1.3 Outline of the Thesis

The remainder of this thesis begins with a theory section covering the relevant properties of pulsed lasers and frequency combs and how two of them can be interfered to produce periodic IGMs and the corresponding RF comb. Chapter 3 summarizes the experimental characterization steps made for both frequency combs and discusses the time stability of the PLL ensuring mutual coherence between both of them. The optical setup is then presented in chapter 4 followed by simulations and experimental characterization of home-made Highly Nonlinear Fibers (HNF) assembled to broaden the spectrum of both combs. DFC measurements and the coherent averaging procedure are then presented in chapter 5. Preliminary absorption and dispersion measurements of an acetylene sample are finally shown to demonstrate the current performances of our DFC system.

# CHAPTER 2 THEORY

This chapter aims to present the relevant theoretical aspects behind DFC measurements starting with mode-locked lasers and their requirements to be considered frequency combs. A DFC theory section details how two frequency combs can be interfered to generate a sequence of RF IGMs and different ways to ensure mutual coherence between both combs are briefly explained.

## 2.1 Light Sources and Their Characteristics

### 2.1.1 Mode-Locked Lasers

In the category of pulsed lasers, there have been many configurations that were developed each with their novelty and limitations. Although they have their own design, the goal remains to generate short, intense and periodic pulses. Gain switching, Q-switching and cavity dumping is a short list of examples of ways to generate pulses and they all rely on temporal modulation of either the gain or losses in the cavity [16]. In the past few decades, a much more efficient method to generate pulsed light was born: mode-locking. To understand mode-locking, one must think about the permitted longitudinal modes oscillating in the laser cavity. If its length is $\ell$, the boundary conditions of the electric field at both ends of the cavity impose that the modes satisfy

$$n\Big(\frac{\lambda_n}{2}\Big) = \ell, \tag{2.1}$$

where $n$ is a positive integer and $\lambda_n$ is the wavelength of the wave associated to $n$. If the group refractive index of the gain medium is $n_g$ (which throughout this thesis is distinguished from the mode number with a subscript), light travels at the group velocity $v_g = c/n_g$ and the frequencies of the longitudinal modes of the cavity are

$$\nu_n = n\Big(\frac{c}{2n_g\ell}\Big) = n\Delta f, \tag{2.2}$$

where $c$ is the speed of light in vacuum and $\nu_n$ is the frequency associated to $n$. In the frequency domain, equation 2.2 exhibits a series of Dirac delta functions spaced-out by $\Delta f = c/(2n_g\ell)$. In the time domain picture, each of these lines represents a sinusoidal component of frequency $\nu_n$ where each mode is paired with a phase $\phi_n$ and an amplitude $A_n$. Since mode-locked lasers have a finite bandwidth $\Delta\nu$, their time domain electric field can be described

by

$$E(t) = \sum_{n_{min}}^{n_{max}} A_n e^{i(2\pi\nu_n t + \phi_n)}, \tag{2.3}$$

where $n_{min}$ and $n_{max}$ refer to the extreme mode indexes of the cavity that are still amplified by the gain medium of the cavity. Put differently, the number of modes in the spectrum $N = n_{max} - n_{min}$ is related to the bandwidth via $\Delta\nu \approx N\Delta f$. Mode-locking a laser consists of *synchronizing* the phase of each temporal mode in a way that they interfere constructively to form periodic pulses at a repetition rate $f_{rep} = \Delta f$. In the time domain, they are separated by a time $\Delta t = 1/f_{frep}$ attributed to the photon round-trip time inside the cavity before they exit through an output coupler. Mode-locking yields destructive interference of the modes in between the pulses such that the instantaneous intensity at those moments is zero. The mean power remains the same as if there was no locking, but the energy is now coherently stored in short and $\sim N$ times more powerful light pulses.

### Mode-Locking Schemes

Mode-locking is an ensemble of methods that preferentially select a spontaneous bunching of the temporal modes. One may see it as a natural selection process for light pulses. They are generally separated into two main families: active and passive mode-locking. Active mode-locking means an external signal or modulation must be applied to a cavity component to mode-lock the laser. An active mode-locking component, such as an electro-optic switch, is designed to modulate the modes inside the cavity at a frequency corresponding to its inverse round-trip time. This modulation of a particular mode sheds energy to its adjacent modes in a way to yield equally spaced-out phase-locked modes and generate short coherent pulses [16]. For passive mode-locking, no external input is needed and short pulses are generated by simply having an appropriate passive component in the cavity. One passive mode-locking technique is Kerr lensing where the gain medium in the cavity has an intensity-dependent refractive index [17]. When the spatial modes are focused in the gain medium, the spatial energy distribution is denser towards the center than at its edges, creating a spatial lensing effect. Laser cavities relying on Kerr lensing are engineered to be unstable for CW operation with hard or soft apertures to favour pulsed operation, a condition met only when the phase is locked [18, 19]. Another type of passive mode-locking method is to use a Semiconductor Saturable Absorber Mirror (SESAM) in the cavity. These mirrors have an intensity-dependent absorptivity such that they absorb light pulses below a threshold intensity; past this point, the reflectivity is significantly greater. By introducing a SESAM in the cavity, there is a preference for original pulses that are more intense, i.e. when the phase of the longitudinal modes are well synchronized [16].

**Pulse Duration**

There are three main aspects that control the duration of the individual pulses of a mode-locked laser. Since their generation is based on interference of all the cavity modes amplified by the gain curve, the greater the number of modes that are constructively added together, the shorter the pulse can become. This may be seen as the time domain analog of the spatial interference pattern occurring when illuminating an array of narrow slits; the Full-Width Half-Max (FWHM) of each principal maximum gets progressively narrower when increasing the number of illuminated slits. In general, the pulse duration $\tau$ is inversely proportional to the bandwidth of the laser and has a fundamental minimum value known as the Fourier-Transform Limit (FTL):

$$\tau \Delta\nu \geq a, \tag{2.4}$$

where $a$ is a constant that depends on the pulse shape. For Gaussian and sech$^2$, two of the most common pulse shapes in ultrafast photonics, this constant is 0.441 and 0.315, respectfully [20]. Even if it is not the most significant factor, this highlights how the pulse shape can contribute to the length of the pulse. To reach the FTL, a large number of modes is not sufficient. For an arbitrary pulse shape and number of modes, the shortest possible pulses are achieved when all modes are well synchronized inside the pulses. This means the arrival time of all the modes at the output coupler of the laser must be frequency-independent. Otherwise, the pulses get broadened in time due to dispersion. Quantitatively, $\phi_n$ can be seen as a discrete version of a continuous spectral phase $\phi(\omega = 2\pi\nu)$ which is often described through its Taylor series:

$$\phi(\omega) = \phi_0 + \frac{\partial\phi}{\partial\omega}\Big|_{\omega_0}(\omega - \omega_0) + \frac{1}{2}\frac{\partial^2\phi}{\partial\omega^2}\Big|_{\omega_0}(\omega - \omega_0)^2 + \frac{1}{6}\frac{\partial^3\phi}{\partial\omega^3}\Big|_{\omega_0}(\omega - \omega_0)^3 + \dots\,, \tag{2.5}$$

where $\omega_0$ is the central angular frequency and $\phi_0$ represents an overall phase shift that is common to all the modes. This global phase is meaningful only when considering the electric field since it is lost when measuring its intensity. The second term applies an overall Group Delay (GD) on the whole pulse (field and thus envelope) while preserving the initial width of the pulse. Such delays are accumulated whenever a pulse enters a medium other than vacuum because its group velocity is reduced from $c$ to $c/n_g$ while being inside the material. By expressing the spectral phase through the frequency-dependent wavenumber $k(\omega)$ and a propagation length $L$: $\phi(\omega) = k(\omega)L$, it is clearer how those delays are acquired for a specific material:

$$\mathrm{GD} = \frac{\partial\phi}{\partial\omega} = L\frac{\partial k}{\partial\omega} = \frac{L}{v_g}, \tag{2.6}$$

where GD is the additional time the wave takes to travel through a thickness $L$ and the group velocity is defined as the first derivative of the angular frequency with respect to the wavenumber. In most materials, the group velocity is also frequency-dependent, so the delay acquired according to equation 2.6 is different for all frequencies. This can lead to laser pulses that have duration above the FTL because the interfered modes are not perfectly synchronized, a phenomenon called Group Delay Dispersion (GDD). It is often referred to as *chirp* since every component arrives at a different time. Mathematically, GDD is defined as the second-order derivative in equation 2.5:

$$\text{GDD} = \frac{\partial^2 \phi}{\partial \omega^2} = L \frac{\partial}{\partial \omega} v_g^{-1}. \tag{2.7}$$

For Gaussian pulses of $\tau_0$ FTL durations, dispersion stretches them in the following way:

$$\tau = \tau_0 \sqrt{1 + \left(4\ln(2) \frac{\text{GDD}}{\tau_0^2}\right)^2}, \tag{2.8}$$

where both $\tau$ and $\tau_0$ are FWHM pulse durations. Equation 2.8 also shows how dispersion has an even greater effect on shorter FTL durations, highlighting yet another challenge when working with broadband sources (see equation 2.4). In the Taylor expansion of the spectral phase, the superior order terms also contribute to the stretching and deformation of the pulses in an increasingly complex way. In the case of Third Order Dispersion (TOD), the third derivative of the spectral phase, it causes an asymmetric pulse and trailing secondary pulses in some cases. This is the result of the interference of the red and blue parts of the pulse that are not travelling at the same speed. Above the third order, the modes' velocity distribution in the pulse is non-linear, yielding even more exotic pulse shapes.

### Pulse Characterization

It is fairly easy to measure the spectrum of a pulsed laser using a spectrometer, but accessing its spectral phase is not as trivial. Some form of interferometry is mandatory, but linear auto-correlators like Michelson interferometers are insufficient since they provide no information on the spectral phase [16]; the solution lies in the combination of interferometry and nonlinear effects. Even so, some nonlinear interferometer designs (e.g. intensity auto-correlators) are only able to provide a rough estimation of the pulse width and spectral phase shape. One of the most popular and faithful ways to fully characterize a pulsed laser is with Frequency-Resolved Optical Gating (FROG), a type of nonlinear auto-correlator recording the spectrum of the source when optically gated with a short, known delayed pulse. In the case of Second-Harmonic Generation-FROG (SHG-FROG), the gate is the unknown pulse itself and the

measured spectrum as a function of the applied delay $\tau$ gives a two-dimensional spectrogram [21]:

$$I_{FROG}(\omega,\tau) = \left| \int_{-\infty}^{\infty} E_{SFG}(t,\tau) e^{-i\omega t} dt \right|^2, \tag{2.9}$$

where $E_{SFG} = E(t)E(t-\tau)$ is the Sum-Frequency Generation (SFG) time signal resulting from the mixing of the pulse $E(t)$ and the delayed gate $E(t-\tau)$; the squared magnitude of the Fourier transform of $E_{SFG}$ (or spectrum) is measured with a spectrometer. Experimentally, the spectrogram can be acquired with the setup depicted in figure 2.1 where the laser is separated in two with a Beam-Splitter (BS) and a delay $\tau$ is applied to one branch. Both copies are separately collected by another BS and focused in an SHG crystal where they generate their own SHG signal. When they temporally and spatially overlap in the crystal, a third SFG signal is produced and measured for every delay to yield $I_{FROG}(\omega,\tau)$.

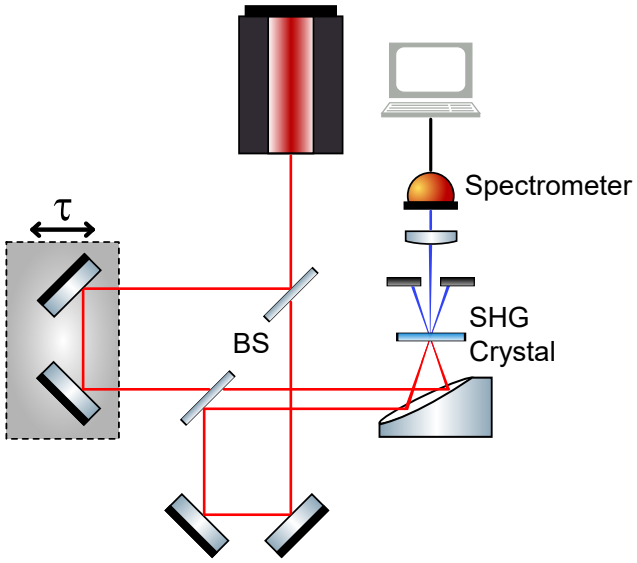


Figure 2.1 Typical SHG-FROG experimental setup. The laser to be characterized is split in two equal parts with a BS where one of them is sent to a variable delay stage. Both paths are collected by a second BS and focused at the same point in a SHG crystal by a parabolic mirror. Both SHG signals are spatially filtered and the divergent SFG signal is refocused in a spectrometer where its spectrum is recorded as a function of the delay $\tau$.

To uncover the amplitude and spectral phase of $E(t)$ from $I_{FROG}(\omega,\tau)$, a numerical iterative algorithm must be used as there exists no analytical expression for the inversion of equation 2.9. In short, the pseudo-inversion algorithm computes the expected FROG trace for a guess spectrum and spectral phase and adjusts them until the simulated FROG trace converges toward the measured one. SHG-FROG measurements can retrieve an accurate pulse duration

and spectral phase, but don't provide the sign of the chirp. This ambiguity comes from the choice of the gating pulse: for SHG-FROG, delays of $\pm\tau$ give the same spectrum since the gating pulse is also the pulse to characterize. If the gating pulse is such that delays of $\pm\tau$ doesn't generate the same SFG spectrum, the sign of the chirp may be recovered. However, there is an easy workaround for this issue with time-symmetric spectrograms and it consists of adding an optic with a known sign of dispersion and check if it compresses or chirps even more the pulse [22].

### 2.1.2 Frequency Combs

As discussed in section 2.1.1, the spectrum of an ideal mode-locked laser is composed of many phase-locked monochromatic lasers, all equally spaced-out by $f_{rep}$, effectively forming a *frequency comb*. In fact, the longitudinal modes of a real frequency comb are slightly different than what is suggested by equation 2.2. In general, the whole spectrum is shifted towards higher frequencies by an amount called Carrier-Envelope Offset (CEO) frequency $f_{ceo}$, such that any comb tooth of a frequency comb can be accessed with

$$\nu_n = f_{ceo} + n f_{rep} \ , \tag{2.10}$$

where by construction, $0 \leq f_{ceo} < f_{rep}$. Figure 2.2a illustrates a typical frequency comb spectrum. In the frequency domain, the effect of $f_{ceo}$ is relatively straightforward, but its name is best explained in the time domain. If a frequency comb has a null $f_{ceo}$, its spectrum will, of course, be made of exact integer times the repetition rate of the laser. In the time domain, this results in a non-varying pulse-to-pulse Carrier-Envelope Phase (CEP). Whenever $f_{ceo}$ is non-zero, the CEP from pulse to pulse will change by $|\Delta\phi| = 2\pi\frac{f_{ceo}}{f_{rep}}$ [23], as depicted in figure 2.2b. The sign of $\Delta\phi$ depends on if $f_{ceo}$ is greater than $f_{rep}/2$ or not. Another way to visualize the effect of $f_{ceo}$ is that the frequency at which the CEP comes back to a specific value is $\min(f_{ceo}, f_{rep} - f_{ceo})$.

In general, dispersion in the cavity is the cause for non-zero $f_{ceo}$. More precisely, the differences between the group and phase velocities of the electric field are behind this frequency shift. The nuance between the two is that the group velocity is the speed at which the envelope of the pulse travels and the phase velocity is the speed of its carrier wave. Whenever they are not balanced, the oscillating field accumulates a phase difference $\Delta\phi$ described above [24–27].

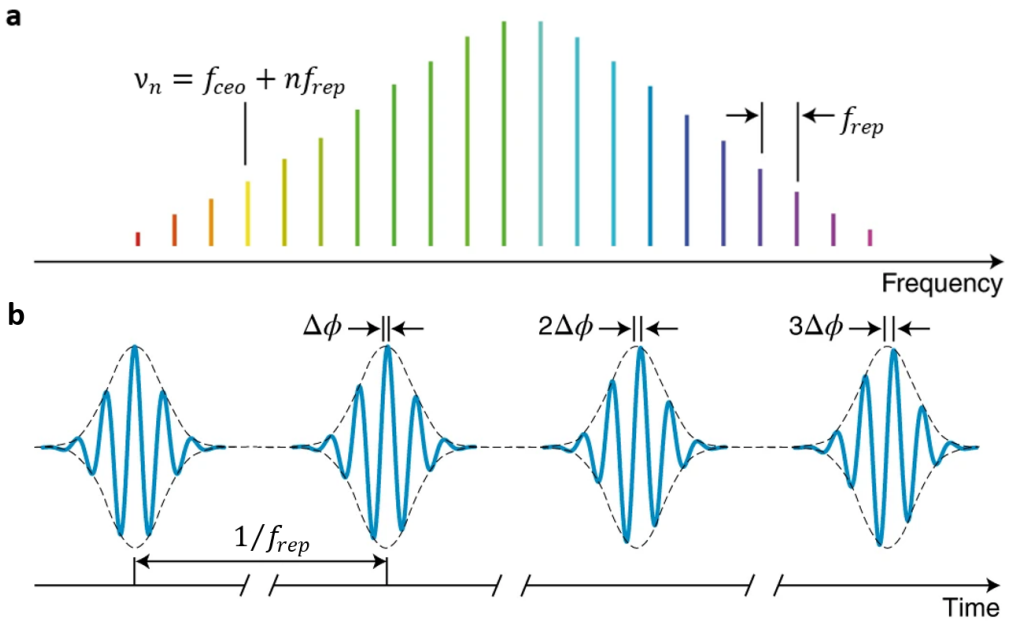


Figure 2.2 Frequency comb representation in the a) frequency domain and b) time domain. $f_{rep}$ is the repetition rate of the laser and its inverse is the time separation between the pulses. $\nu_n$ is the frequency of the $n^{th}$ comb tooth. A pulse-to-pulse CEP variation $\Delta\phi$ is associated to a non-zero $f_{ceo}$. Schematics adapted from [1] with permission.

### Time Stability of Frequency Combs

In ultrafast photonics, the frequency comb label is reserved to *stabilized* mode-locked lasers [28]. More often than not, the repetition rate of a frequency comb is stabilized, where as for $f_{ceo}$, it is not always the case. Even with a stabilization scheme, these degrees of freedom can fluctuate in time and alter the optical spectrum in the following way:

$$\nu_n + \Delta\nu_n(t) = (f_{ceo} + \Delta f_{ceo}(t)) + n(f_{rep} + \Delta f_{rep}(t)). \tag{2.11}$$

As depicted in figure 2.3, a time-dependent $f_{ceo}$ leads to a rigid shift in time of the spectrum, while fluctuations in $f_{rep}$ appear as accordion-like behaviour in the spectrum.

Fluctuations showed in figure 2.3 arise from various phenomena surrounding the laser cavity. Repetition rate fluctuations are often caused by external vibrations, pump laser intensity fluctuations and varying environmental conditions such as temperature, pressure and humidity for example [23,29,30]. Since they all contribute to the effective length of the cavity, using frequency combs as precise metrology tools requires correcting for these effects in real time. Common processes or components to stabilize the repetition rate are temperature control, Electro and Acousto-Optic Modulators (EOM, AOM) [31–33] and Piezoelectric Transducers

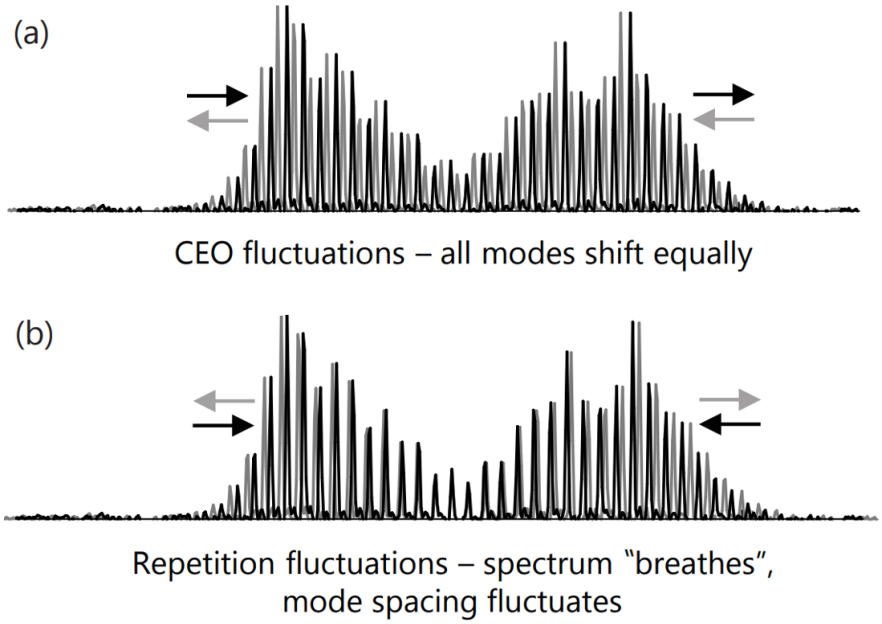


Figure 2.3 Effect of time fluctuations on a frequency comb spectrum. Figure adapted from [2] with permission.

(PZT) [26, 33]. They are often combined to separately correct for slow ($\sim$ sub-kHz range) and fast (up to a couple 100 kHz) fluctuations. They all need a real-time measurement of the repetition rate for real-time feedback control. Luckily, this can be easily done with only a fast photodetector [25,26,34] where its output signal is fed to a repetition rate stabilization loop.

On the other hand, measuring and changing $f_{ceo}$ is trickier. $f_{ceo}$ cannot be directly measured since it is not part of the optical spectrum, while in the time domain it would require to monitor CEP slips on a pulse-by-pulse basis. A clever alternative known as $f$-to-$2f$ interferometry was proposed by Telle et al. [25] to circumvent this challenge. It requires an octave-spanning frequency comb, meaning a frequency and its second harmonic must be part of the spectrum. As shown in figure 2.4, the idea is to interfere the blue part of the octave-spanning comb ($\nu_2$) with the second harmonic of its red part ($2\nu_1$). By doing so, an easily detectable beat frequency is produced at $f_{ceo}$. Other beats at $f_{rep} - f_{ceo}$, $f_{rep} + f_{ceo}$, $2f_{rep} - f_{ceo}$, etc. can also be generated during this process, but only beats below $f_{rep}$ are relevant. A low-pass analog filter can be used to discard redundant beats. Even so, the remaining $f_{ceo}$ and $f_{rep} - f_{ceo}$ beats are ambiguous: unless $f_{ceo} = 0$ or $f_{rep}/2$, it is not clear if $f_{ceo}$ is smaller or greater than $f_{rep}/2$. With continuous monitoring of these beats, this is rarely an issue as $f_{ceo}$ can be set to zero through another closed loop with the $f$-to-$2f$ signal as an input. Instead of adjusting the length of the cavity, this second loop usually tunes the pump

current of the laser and/or the alignment of dispersive optics in the cavity to counter $f_{ceo}$ fluctuations [25–27]. Another way to achieve $f_{ceo}$-free combs is through Difference-Frequency Generation (DFG) between two spectral components issued from the same source. Since they have the same $f_{ceo}$, it will be cancelled with this non-linear process and yield phase-stable pulses [35–37].

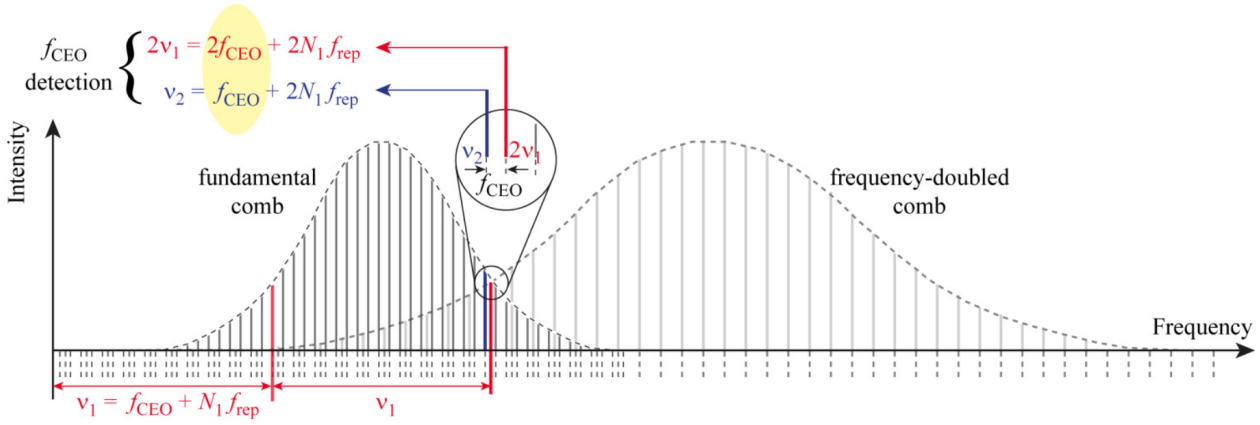


Figure 2.4 $f$-to-$2f$ interferometry principle. An octave-spanning frequency comb containing frequencies $\nu_1$ and its second harmonic $\nu_2$ is split in two parts. One of them is frequency-doubled such that $2\nu_1$ falls within $f_{rep}$ of $\nu_2$ to generate measurable RF beats at $f_{ceo}$ and $f_{rep} - f_{ceo}$ when interfered with the fundamental comb. Figure taken from [3] with permission.

Octave-spanning frequency combs are not trivial to realize and non-linear effects such as Supercontinuum Generation (SCG) are often needed, but they are the key to reach fully stabilized frequency combs. Moreover, some optical processes like High-Harmonic Generation (HHG) and compression are $f_{ceo}$-dependent so it is crucial to have this information at hand [38].

## 2.2 Spectroscopy

The ability to accurately control a frequency comb's parameters opens up many opportunities in terms of precision measurements since the absolute frequency of every mode is known. Frequency combs can be viewed as rulers for light and fields like spectroscopy always aim to improve the available resolution and exactitude to better identify unknown samples. Frequency and time domain detection spectroscopy are introduced in order to highlight their advantages and limitations. DFC interferometers are then introduced through a comparison with Michelson interferometers.

### 2.2.1 Frequency Domain Detection

The simplest way to do spectroscopy of a sample is to send a characterized, broadband light source through the analyte and collect the transmitted light in a spectrometer. By comparing the transmitted and original spectra, the absorption features of the sample appear and it is possible to identify it. In frequency-domain detection spectroscopy, the spectrometer contains a (or a combination of) dispersive optic(s) to spatially split the incoming light toward an array of photodiodes where each is used to sample a portion of the power spectral density. In such spectrometers, the spectral resolution is mostly set by its angular dispersion and the density of detectors: the greater the dispersion and number of detectors, the better resolution can get. Most commercial gratings and prism spectrometers designed for optical frequencies have a sub-nm to few nm resolution. While they are great to provide an overall idea of a spectrum, it is not sufficient to resolve frequency comb teeth or narrow absorption lines of unknown samples. There exists high-resolution frequency-domain detectors such as Virtually Imaged Phased Array (VIPA) dispersers or Optical Spectrum Analyzers (OSA) that reach few GHz resolutions [39,40], resolving individual comb teeth of faster repetition rates frequency combs. However, shifting the detection in the time-domain opens the door to even better resolution in some cases.

### 2.2.2 Michelson and DFC Interferometers in the Time Domain

The goal with time-domain detection spectroscopy is still to access the frequency spectrum of the source or sample, except that the measurement is a signal in time which is Fourier transformed to get to the spectrum. There are various ways to do so and one of the most popular is with a Michelson interferometer, which turns out to be extremely similar to DFC interferometers. This presents the time-domain similarities between both methods via figure 2.5, where the top row describes the principle of Michelson interferometers and is compared to the DFC picture in the second row.

The Michelson-Morley interferometer enables FTIR spectroscopy in the time domain by interfering two delayed copies of a same light source and recording the autocorrelation signal, as shown in figure 2.5a. A motorized mechanical stage is typically used to apply a delay between the two copies and a detector records the resulting intensity for all separate stage positions. By varying this delay, a signal known as an IGM is produced and shown on figure 2.5b. To properly sample an IGM, the step size of the stage must be at most of the longest wavelength of the source divided by two to respect the Nyquist sampling condition. This specific case is shown with coloured dots on figures 2.5a and b for a few points surrounding zero-path delay. In general, the sampling is set to be slightly more frequent than the Nyquist

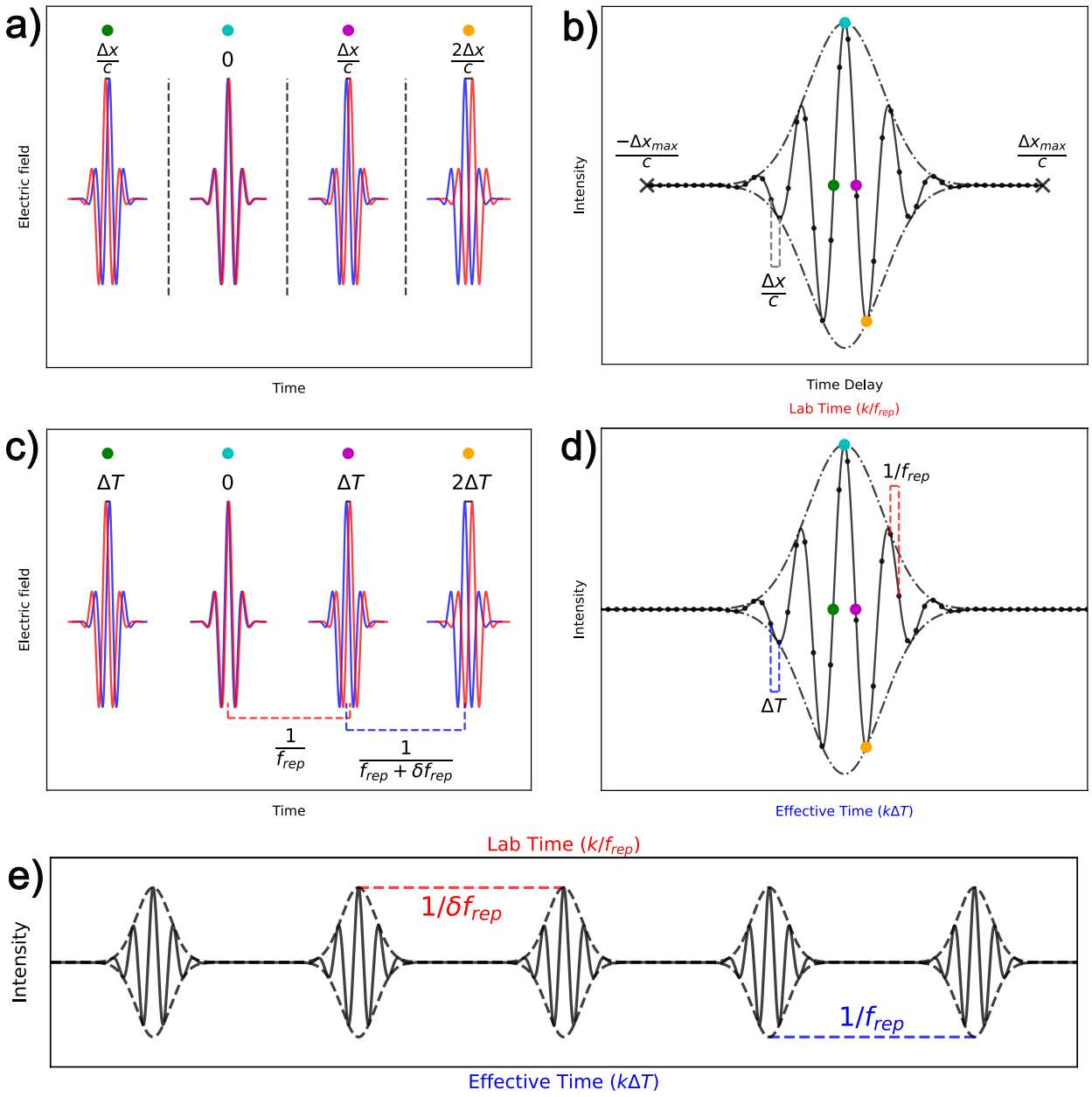


Figure 2.5 a) Interference of two delayed pulses in a Michelson interferometer through a varying optical path delay $\Delta\tau = \Delta x/c$. The dashed lines represent the dead times between the separate measurements. b) Generated interferogram with a Michelson interferometer where each measurement (black dots) is separated by $\Delta x/c$ and covers the total range of the delay stage. Coloured data points in sub-figures b) and d) correspond to events of the same colour in sub-figures a) and c) where the phase difference between the pulses are -$\pi/2$, 0, $\pi/2$ and $\pi$. c) Interference of pairs of delayed pulses in a DFC interferometer resulting from the different repetition rates of the frequency combs. d) Generated interferogram with a DFC interferometer. Each point is acquired after a lab time of $1/f_{rep}$ while the effective time delay between the pulses is increasing by $\Delta T$ e) Periodic interferograms repeating after a lab time of $1/\delta f_{rep}$ (which also corresponds to an effective time delay of $1/f_{rep}$) for a DFC interferometer.

condition, a scenario showed with black dots. Also, all delay stages have a finite travel range, hence a maximum delay $\Delta x_{max}/c$ that limits the available resolution in the frequency domain. In addition to the measured oscillating signal, the IGMs have an envelope that is directly related to the shape of the spectrum in the frequency domain: according to the Wiener-Khinchin theorem, the Fourier transform of the IGM yields the spectrum of the source [16].

However, this technique has multiple inherent challenges. The mechanical stage used to apply the delays is prone to external vibrations and travels slowly. This results in important dead times between each stage position such that a total measurement generally takes on the order of seconds to minutes depending on the required SNR. Moreover, the finite range of stage automatically sets a limit on the reachable frequency resolution in the spectrum. There exist high-resolution FTIRs [41, 42], but inevitably require long delays and measurement times.

These challenges are addressed with DFC interferometers all while recycling the advantages and intuitive functioning of Michelson interferometers. The idea is to interfere two frequency combs of slightly different repetition rates in a way as to mimic the delays between the pulses like in a Michelson interferometer, as seen on figure 2.5c. Since neither laser may be exactly the same, the measurement is now a cross-correlation signal instead of an autocorrelation. At some point in time, both pulses become synchronized and the delay between them is null. The time difference between the very next pulse of each laser will be

$$\Delta T = \frac{1}{f_{rep}} - \frac{1}{f_{rep} + \delta f_{rep}} = \frac{\delta f_{rep}}{f_{rep}(f_{rep} + \delta f_{rep})}, \tag{2.12}$$

where $f_{rep}$ is the nominal repetition rate of both frequency combs and $\delta f_{rep}$ is their detuning. Then, the delay between the adjacent pulse pairs is progressively increasing as integers $k$ times $\Delta T$, which is exactly the same as having a constant step size in a Michelson interferometer. According to equation 2.12, the delays between the pulses are exclusively set by both repetition rates, where in most cases, the detuning is adjustable. Moreover, the delay difference $\Delta T$ determines the maximal bandwidth of the incoming sources. For the pulse pairs shown in figure 2.5c, if $\Delta T$ is set any larger (by increasing $\delta f_{rep}$ for example), the Nyquist sampling condition would not be respected anymore and the pairs of adjacent pulses would interfere only to yield an under-sampled or aliased IGM. A quantitative derivation of the Nyquist sampling condition for DFC interferometers is presented in the frequency domain in section 2.2.3 as it is much more intuitive.

On figure 2.5d, when detected with a low-bandwidth photodiode (capable of resolving $f_{rep}$), the interference of each pulse pair is averaged out to a single point forming an IGM when

the delay between the pulses is scanned. Those delays are often referred to as *effective* times comparatively to the *laboratory* time which specify after how much time another point appears on the IGM and corresponds to the time separation between two consecutive pulses of the same laser, $1/f_{rep}$. Frequency combs of repetition rates on the order of few MHz to few GHz are common for DFC interferometers, so a new data point on the interferogram is added after only a couple nanoseconds or less! Since the delays are no longer limited by the range of a mechanical stage, much larger delays between the pulses are available, which means a considerable increase in the spectral resolution. In fact, effective times eventually get large to the point of starting new IGMs in a periodic way, as presented in figure 2.5e.

To evaluate $t_{sync}$, the laboratory time separation between two consecutive IGMs, the nominal repetition rate is chosen to be a harmonic of the detuning for simplicity. In this scenario, $t_{sync}$ can be expressed in two ways, one from the point of view of each comb:

$$t_{sync} = \frac{k_{sync}}{f_{rep} + \delta f_{rep}}, \qquad t_{sync} = \frac{k_{sync} - 1}{f_{rep}}, \tag{2.13}$$

where $k_{sync}$ is the integer number of pulses the comb with greater repetition rate needs to be synchronized with a pulse of the second comb. The second equation highlights the fact that the slower comb needs one less pulse to reach this condition. Solving for $t_{sync}$ and $k_{sync}$ in equation 2.13:

$$t_{sync} = \frac{1}{\delta f_{rep}}, \qquad k_{sync} = \frac{f_{rep}}{\delta f_{rep}} + 1. \tag{2.14}$$

With $\delta f_{rep}$ detunings commonly on the order of a few kHz, a new IGM is generated every few milliseconds, which is much faster than with a traditional Michelson interferometer. Of course, the effective time corresponding to the beginning of a new interferogram is just $k_{sync}\Delta T = 1/f_{rep}$ (according to equations 2.12 and 2.14) and sets the best spectral resolution of DFC interferometers to $f_{rep}$. This is expected since the spectral sampling points of a frequency comb are spaced-out by their repetition rate.

In the general case where the nominal repetition rate is not a harmonic of the detuning, $t_{sync}$ represents the laboratory time difference between a specific delay between the pulses and the next time it happens. The actual laboratory time before two pulses perfectly overlap could be significantly longer. As long as the Nyquist condition is met, this particular event is not relevant experimentally as the sampling grid of the IGMs would only be shifted.

If $f_{rep}$ and $\delta f_{rep}$ are perfectly stabilized, i.e. independent of time, all interferograms contain the same information. The repetitive IGM signal can thus be averaged to increase SNR [4]. Alternatively, the FFT can be applied to the whole sequence of IGMs to reveal the comb structure of the source. In both cases, it is possible to learn about the coherence time of the DFC source [1, 4], a concept that is further discussed in section 2.2.4.

### 2.2.3 DFC in the Frequency Domain

As seen in the previous section, it is now clear that Michelson and DFC interferometers present strong similarities in the time domain. However, we need to highlight nuances in the frequency domain. For Michelson interferometers using a movable mirror stopping at specific delays, individual measurements in figure 2.5b are made at zero or DC (Direct Current) frequency with slow detectors.

In DFC measurements, both combs present slightly different spectra since they don't have the same repetition rate; this is shown in the frequency domain in figure 2.6 with blue and red optical combs that share the same spectral envelope (black curve) with central frequency $\nu_0$ and near-zero intensity bandwidth $\Delta\nu$. $f_{rep}$ is chosen to be a harmonic of the detuning and $f_{ceo1} = f_{ceo2}$ is set to zero for illustration purposes. Both combs are made to share a non-lasing comb line just outside the lower frequency end of their emission bandwidth and is labelled with a purple zero indicating that their interference registered on a MHz-bandwidth photodiode would produce a DC value corresponding to a peak at zero frequency in the RF spectrum. Toward higher optical frequencies, the very next longitudinal modes of each comb are spaced out by $\delta f_{rep}$ and generate a beat frequency at $\delta f_{rep}$, corresponding to the lowest non-zero peak of the RF spectrum in figure 2.6. The frequency separation between the next two adjacent modes increases to $2\delta f_{rep}$ and produce a beat at this exact RF frequency, and so on. In fact, this Moiré pattern made from the interleaving longitudinal modes of both combs generates a multi-heterodyne beat signal corresponding to an RF comb with components spaced-out by the detuning $\delta f_{rep}$, which is depicted in purple in figure 2.6.

The RF beats can occur from the interference of two adjacent ($n = p$) comb lines to produce lower frequencies between 0 and $f_{rep}/2$. However, beats above $f_{rep}/2$ are also generated in DFC measurements. By considering non-adjacent comb lines ($n \neq p$), the resulting beat frequencies are inevitably greater than $f_{rep}$ and must be filtered out as they represent redundant information. There also exists so-called complementary beats that technically result from the $n = p$ condition, but with a $p$ index great enough to correspond to beat frequencies between $f_{rep}/2$ and $f_{rep}$. According to figure 2.6, they should not be detectable since the spectrum of both frequency combs does not cover beats above $f_{rep}/2$ resulting from the $n = p$ condition.

They are in fact unavoidable since they are already generated under the optical spectra and *complement* the lower beats between 0 and $f_{rep}/2$. For example, the beat under the optical spectrum with a purple label $2\delta f_{rep}$ is generated alongside its complementary beats at higher frequencies $f_{rep} - \delta f_{rep}$ and $f_{rep} - 2\delta f_{rep}$. The grey curve in the RF spectrum depicts a typical low-pass analog filter used to discard beats above $f_{rep}/2$. Additionally, just like an optical comb, the entire RF comb may be shifted by $f_{ceo,RF}$: if $f_{ceo2} - f_{ceo1} \neq k\delta f_{rep}$ and/or $f_{rep} \neq k\delta f_{rep}$ where $k$ is an integer, an RF signal at $f_{ceo,RF}$ may be observed between DC and $\delta f_{rep}$.

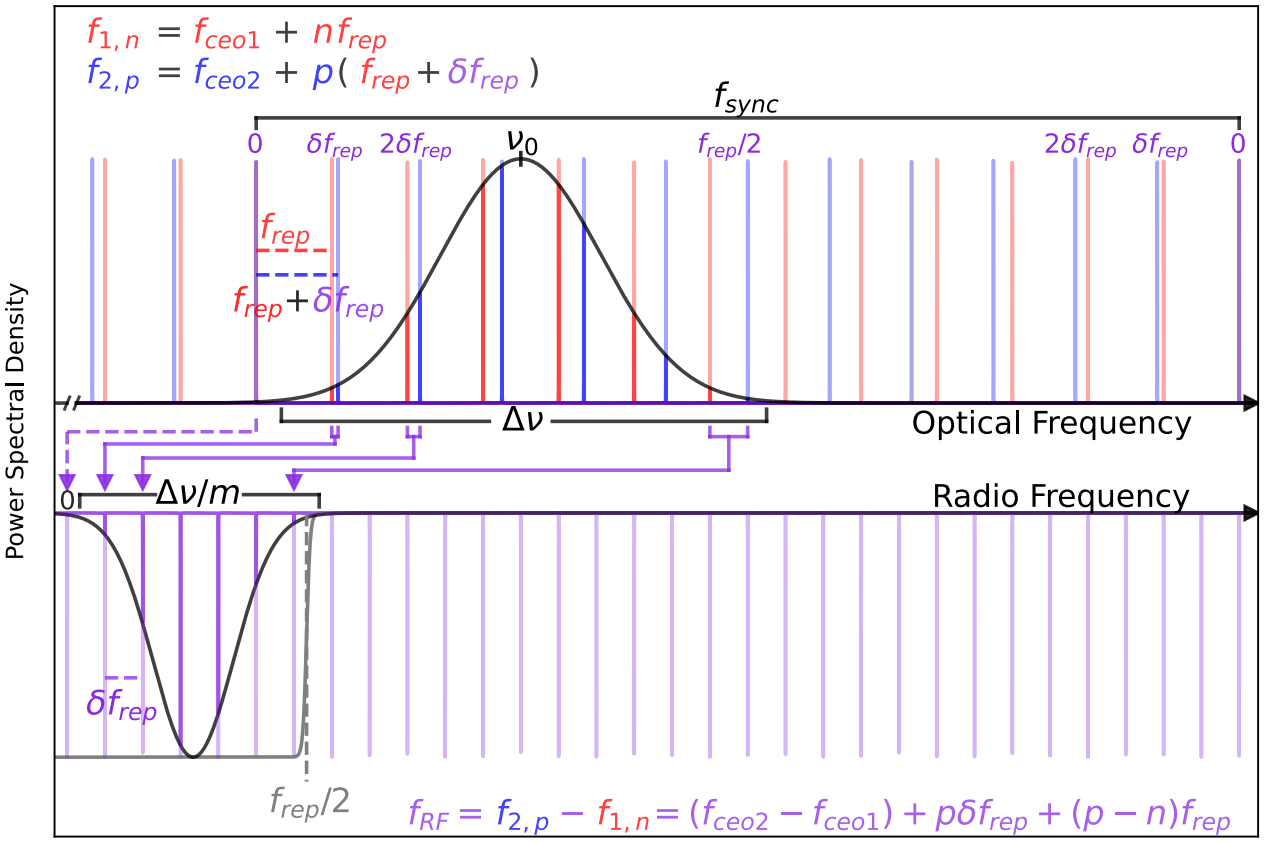


Figure 2.6 DFC in the frequency domain. Optical spectrum of two slightly detuned frequency combs $f_{1,n}$(red) and $f_{2,p}$ (blue) that interfere and produce a radio-frequency comb from beats at integers times the detuning $\delta f_{rep}$ (purple). The central optical frequency of both combs is $\nu_0$ and their optical bandwidth defined at near-zero intensity $\Delta\nu$ must be narrower than $f_{sync}/2$ to ensure a one-to-one optical to radio frequency mapping, where $f_{sync}$ is the optical frequency difference before both lasers share a common comb line. The bandwidth of the radio-frequency comb is compressed by a factor $m$ after being analogically low-pass filtered at $f_{rep}/2$ to preserve beats between adjacent comb lines ($p = n$). This figure presents the specific case where both carrier-offset frequencies are equal to zero and the nominal repetition rate is a harmonic of the detuning.

To ensure a one-to-one mapping of the optical to radio frequencies, it is crucial that the optical bandwidth is adjusted to be narrower than $\Delta\nu_{max} = f_{sync}/2$, where $f_{sync}$ is the separation between two shared comb lines. Half this separation thus forms a mirror plane in the optical frequency domain, where in each half, beats below $f_{rep}/2$ are generated only once each. This condition is often referred to as a Nyquist sampling condition for DFC interferometers and it guarantees that beats below $f_{rep}/2$ are coming from only one region of the optical spectrum. In the simpler case where $f_{ceo1} = f_{ceo2} = 0$ and the nominal repetition rate is a harmonic of the detuning, the calculation of $f_{sync}$ is highly analogous to the one of $t_{sync}$. The comb having a faster repetition rate requires one less comb line than the other comb to reach $f_{sync}$:

$$f_{sync} = n_{sync} f_{rep} \ , \qquad\qquad f_{sync} = (n_{sync} - 1)(f_{rep} + \delta f_{rep}), \tag{2.15}$$

which yield the following when solving for $f_{sync}$ and $n_{sync}$:

$$f_{sync} = f_{rep}\Big(\frac{f_{rep}}{\delta f_{rep}} + 1\Big), \qquad\qquad n_{sync} = k_{sync} = m = \frac{f_{rep}}{\delta f_{rep}} + 1, \tag{2.16}$$

where $m$ may now be seen as a compression factor from optical to radio frequencies, i.e. quantifying how narrower the bandwidth of the RF comb is compared to the one of the optical comb. The maximum optical bandwidth given in terms of the nominal repetition rate and detuning is thus

$$\Delta\nu \leq \frac{f_{sync}}{2} = m\frac{f_{rep}}{2}, \tag{2.17}$$

where the floored integer $m/2$ represents the number of optical modes that are converted to radio frequencies. Even with proper optical filtering, additional analog low-pass filtering is required to remove any frequencies above $f_{rep}/2$ coming from beats between non-adjacent comb lines, including complementary beats. The attenuation past the $f_{rep}/2$ cut-off frequency must be strong enough to completely suppress any unwanted signal and it may be required to use multiple filters to reach this condition. In practice, it is convenient to sacrifice some available bandwidth to get an RF spectrum that goes to near-zero intensity well within the 0 and $f_{rep}/2$ interval as there might be significant $1/f$ noise and/or unwanted signal from individual lasers near DC and beats above $f_{rep}/2$ are pushed towards even higher frequencies where they are better attenuated. Decreasing the detuning is a simple way to get a narrower

RF comb. However, the arrival time of new IGMs is longer (equation 2.16) and the center frequency of the RF comb may change during this procedure such that a part of it may overlap with either DC or $f_{rep}/2$. Manual fine-tuning of $\delta f_{rep}$ can control both the width and center frequency of the RF comb [43, 44], but more sophisticated ways use acousto-optic modulators to shift the spectrum of one optical comb without affecting the width of the RF comb [33].

Thanks to the down-conversion property of DFC interferometers, information stored in optical frequencies is now accessed by measuring much lower, radio frequencies. With repetition rates often on the order of MHz, the need for fast photodetectors and Analog-to-Digital Converters (ADC) is relaxed: flat spectral response between 0 and $f_{rep}/2$ for detectors and sampling rates of at least $f_{rep}/2$ are sufficient and possible without being too costly. With precise measurement of the repetition rate of both combs, the exact optical bandwidth can be retrieved by multiplying the RF bandwidth by the compression factor to yield *relative* optical frequencies. On the other hand, the center frequency found through this calculation should be around $mf_{rep}/4$ which is only a couple of THz, far from the actual central frequency. This compressing and shifting property washes away the exact position of the central optical frequency of both spectra and calls for a separate, absolute reference frequency measurement often using stable narrow-linewidth CW lasers [4, 33, 44, 45].

Additionally, an inversion of the RF spectrum with respect to $f_{rep}/4$ may be observed depending on the maximal optical bandwidth $\Delta\nu_{max}$ and central optical frequency $\nu_0$. For two optical spectra with bandwidth that respect the Nyquist condition, their central frequency could be such that the low optical frequencies are mapped to low RF frequencies (situation showed on figure 2.6). The other possible case is the opposite where low optical frequencies are mapped to higher RF frequencies and vice versa. Mathematically, the parity of the integer division $\lfloor \nu_0/\Delta\nu_{max} \rfloor$ determines if an inversion has happened: there is one only if the result is odd.

To do spectroscopy with either a Michelson or DFC interferometer, a sample can be placed in the light path after the sources are combined in a so-called symmetric (or collinear) configuration, as in figure 2.7a. Alternatively, figure 2.7b shows how the sample can be placed such that a single arm (or frequency comb) of the interferometer goes through it to form an asymmetric (or dispersive) configuration [46]. In both cases, a separate measurement without the sample is mandatory to act as a reference. When both arms (or lasers) travel through the sample, its absorption spectrum in intensity can be extracted. In the time domain, the real part of the sample's response function shows up as a Perturbed Free Induction Decay (PFID) signal [47]. Its imaginary part is not accessible in the collinear configuration and the resulting

IGMs are symmetrical with respect to zero delay; its only effect is to apply a global arrival time delay on the IGM. For DFC interferometers, IGMs recorded with this scheme may be asymmetric due to differences between both spectra and appear as a cross-correlation [48] signal instead of a symmetrical autocorrelation. In the dispersive configuration, only one path of the interferometer is affected by absorption and frequency-dependent GD. When interfered with the other source, the generated IGMs are expected to be asymmetric with respect to zero-delay and phase information of the sample is recovered alongside with its amplitude absorption spectrum. Dispersion and absorption are the two sides of a same coin as they are related through Kramers-Kronig relations [16]. Nevertheless, direct measurement of the phase enables dispersion characterization of a sample, while the symmetric configuration is more robust against environmental fluctuations and sufficient if only absorption features are of interest [4].

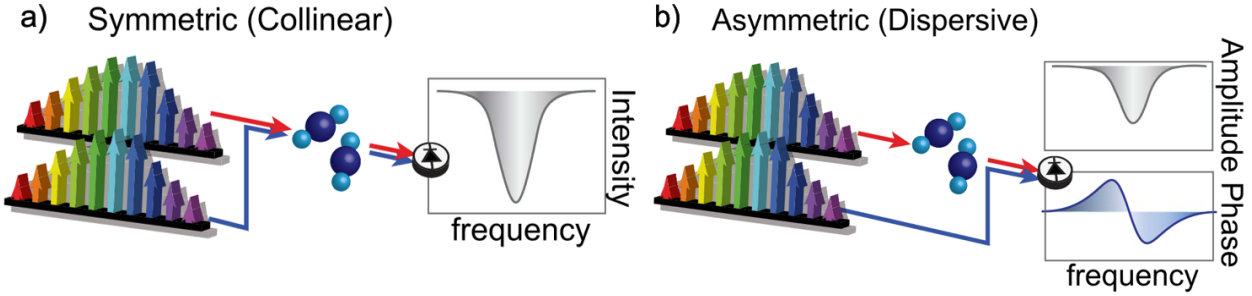


Figure 2.7 a) Symmetric (collinear) and b) asymmetric (dispersive) schemes for spectroscopic measurements of an unknown sample. With either a Michelson or DFC interferometer, both sources go through the sample in the symmetric scheme to yield the intensity absorption spectrum. Both the amplitude absorption spectrum and phase shifts of the sample are measured when only one source sees the sample. Figure adapted from [4] with permission.

### 2.2.4 Coherence of Dual-Frequency Combs Sources

There exists three main families of DFC sources and they are classified according to their level of mutual coherence, i.e. how stable they are in time during measurements. Each category has its set of advantages and challenges, and trades between high SNR, accuracy and resolution with complexity and cost of the experimental setup [4].

#### Fully Referenced Frequency Combs

The ideal DFC source for spectroscopic measurements is made of two fully referenced frequency combs, meaning they both have a PLL to actively stabilize their repetition rate and

$f_{ceo}$s which rely on external stable and narrow-linewidth CW lasers as absolute references. Such CW lasers are commercially available and can be stabilized with high-finesse cavities. The absolute references are interfered with a part of the spectrum of the frequency combs and the lowest frequency beat is used as an input to either tune $f_{rep}$ or $f_{ceo}$ [33, 49]. Owing to their long coherence times, such DFC schemes result in a fluctuation-free sequence of IGMs that can be coherently averaged to considerably increase the SNR. Moreover, the external optical references provide the exact shift that must be applied to the frequency axis once it's been converted to relative optical frequencies. The reason why not all DFC systems are fully referenced is simply because of their cost and complexity. The additional lasers imply more characterization and challenges and form complicated setups with many feedback loops, making them susceptible to small environmental perturbations.

**Mutually Coherent Frequency Combs**

Although the external references extend the coherence time of the DFC setup and provide exact optical accuracy, they are not mandatory for all spectroscopic measurements, especially when the absorption linewidth of the analyte is much broader in comparison to the comb linewidth. DFC systems with PLLs to ensure coherence between both combs that operate without external references exist and are often referred to as mutually coherent frequency combs. Coherent averaging is still possible, but numerical post-processing algorithms may be required to correct for the drifts observed in the periodic IGM sequence. As described below in section 3.4, the system used in this project falls in this category as a single PLL is used to maintain a stable repetition rate difference $\delta f_{rep}$ and is combined with a correction procedure to account for the remaining fluctuations.

**Free-Running Frequency Combs**

Even simpler DFC systems are reported and rely on two free-running combs, meaning there are no PLLs to ensure mutual coherence between the combs. Without any form of post-measurement corrections, coherent averaging is limited as the coherence time is much shorter than with more robust configurations using PLLs. Yielding much simpler experimental setups, proof-of-principle systems with free-running combs have shown the first DFC measurements [50, 51], but intrinsically more stable combs combined with proper phase corrections extend their effective coherence time and proceed to coherent averaging [45, 52].

# CHAPTER 3 CHARACTERIZATION OF FREQUENCY COMBS

As discussed in section 2.2.4, the DFC system must meet many requirements for the measurements to be precise, exact and have high SNR. For this project, we use a custom system designed by NKT Photonics which is composed of two mutually coherent Origami LP passively mode-locked frequency combs made of a hybrid cavity relying on fiber and solid-state technology. The sources are centered at 1570 nm and have a 100 mW main output and 2 mW tap-out port for monitoring and stabilization purposes. Both combs have a stabilized repetition rate with unstabilized $f_{ceo}$ and were characterized in many ways before combining them to perform DFC spectroscopy. Their pulses are characterized through SHG-FROG measurements and the time stability of their two degrees of freedom $f_{rep}$ and $f_{ceo}$ is evaluated. Most importantly, the system's ability to maintain a specific repetition rate difference is confirmed.

## 3.1 SHG-FROG Measurements

SHG-FROG measurements are performed on both the Master and Slave frequency combs to confirm the spectrum provided by the manufacturer and learn about the spectral phase shape. These measurements are also useful to evaluate if the combs are suited for $f_{ceo}$ measurements (discussed in section 3.3) since compressed pulses are required.

The experimental setup is the one depicted in figure 2.1 were two 50/50 BS are used to split and then recombine optical pulse trains. A computer-controlled optical delay line is used for the analysis of the SFG signal as a function of the temporal delay between the pulses and their copies, yielding pulse characterization information. Since the splitting ratio of the BSs is polarization-dependent, a Half-Wave Plate (HWP) is placed before entering the FROG setup to adjust the polarization. Its optimal orientation yields equal intensities in reflection and transmission, a situation that produces maximal SFG signal when both beams are focused in the type-I SHG crystal, made of Beta Barium Borate (BBO) in our case. The thickness of the crystal is 50 $\mu$m and it is cut at an angle of 19.8°. The parabolic mirror used is silver-coated to minimize losses and has a reflective focal length of 25.4 mm and the BBO crystal is placed at the focal point. Both SHG signals coming from individual beams are spatially filtered with a tight aperture that lets through the SFG signal. Instead of using a lens to focus the divergent SFG signal, a concave mirror at a near-normal incidence is placed at a distance longer than its focal length to focus the light in a Czerny-Turner spectrometer (Thorlabs CCS175) with an integration time of 80 ms. It records the SFG spectrum for all delays $\tau$ that are added

via a motorized actuator (Thorlabs Z825B) pushing a linear stage supporting two mirrors. For each delay, 10 spectra are measured and averaged to gain a $\approx \sqrt{10}$ factor in SNR since noise from different spectra is expected to be uncorrelated [53]. In principle, this could be achieved by increasing the integration time of the spectrometer, but we observe sub-linear signal scaling with integration times longer than 100 ms due to sampling and software errors and implemented this alternative to yield an effective integration time of 800 ms.

Figure 3.1a shows the FROG trace acquired with the Master laser where we can clearly see the main feature centered at 0 fs accompanied by much dimer peaks at ±600 fs for frequencies around 383 THz. This is the signature of a pulse that contains a main and secondary pulse that are separated by ≈600 fs. With the gating function being the pulse itself in SHG-FROG, features at ±600 fs correspond to situations where the main pulse of one copy is temporally synchronized with the secondary pulse of the other branch. The main feature in figure 3.1a represents the situation where the main and secondary pulses of each branch overlap. Additionally, the expected symmetry with respect to zero delay is visible and makes it impossible for us to tell which pulse is leading. The same effect prevents us from finding the sign of dispersion.

To extract the spectrum and its spectral phase out of the FROG trace, we use the Common Pulse Retrieval Algorithm (COPRA) [54]. Prior to the retrieval, points in the normalized FROG trace that have a relative intensity inferior to 0.05 are forced to 0 to take out remaining noise and facilitate the retrieval. This acts as many two-dimensional step-function intensity filters which make the retrieved pulse and spectrum smoother. Apodizing the FROG trace may introduce artifacts coming from this abrupt filtering, but they should be unnoticeable compared to the effects of no filtering at all. Using appropriate smoother filters may improve the exactness of the retrieval even more [55].

Figures 3.1b shows the retrieved spectrum and its spectral phase of the Master laser, while 3.1c displays the envelope of the retrieved pulse in the time domain alongside its FTL. The spectrum is well behaved for frequencies below 191 THz, after which clear, periodic dips separated by ≈1.6 THz appear. Interestingly, the inverse of this interference frequency is ≈600 fs, the time separation between the main and one of the secondary features in the FROG trace. Moreover, it appears there are two regimes in the spectral phase. On the lower frequency side, the phase is roughly linear with slight higher orders which indicates that this part of the spectrum is near-transform limited. For higher frequencies higher than 191 THz, the spectral phase presents large jumps and are expected for such a spectrum. In the same spectral region, we notice what resembles to be GDD and TOD.

In the time domain, the retrieved pulse is comprised of a main, virtually FTL (90.2 fs vs 86

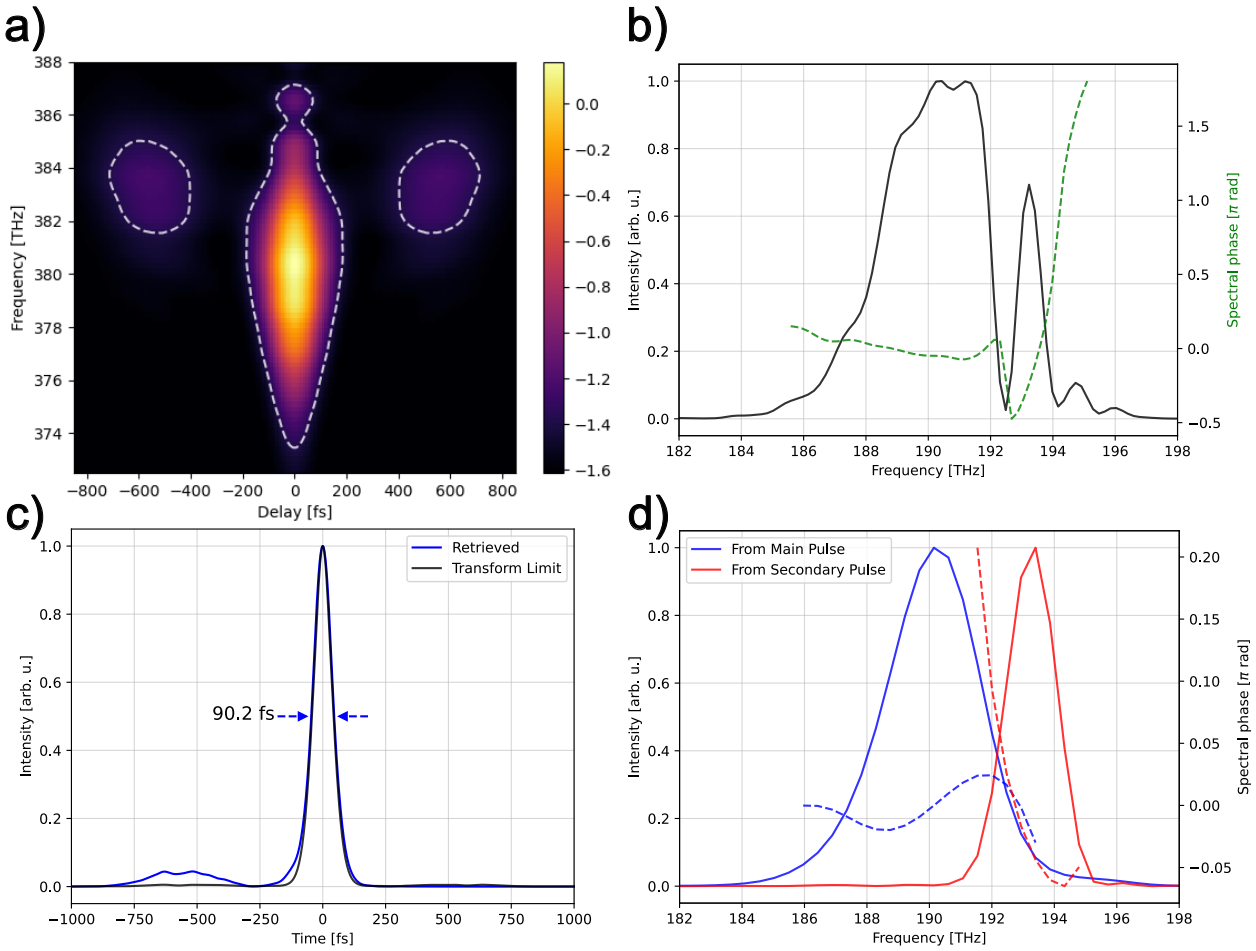


Figure 3.1 a) SHG-FROG trace of the Master laser with a spectrometer integration time of 80 ms where 10 points per delay are acquired. The intensity is plotted on a logarithmic scale and dashed contour lines reveal dimer features. The spectrogram is sampled for delays separated by $2\mu m/c$ covering a total range of $\pm 400\ \mu m/c$. b) Retrieved spectrum (black, full) and spectral phase (green, dashed) of Master laser. c) Retrieved pulse with FWHM of 90.2 fs (blue) compared to its FTL (black). d) Spectra (full) and spectral phases (dashed) of the main retrieved pulse (blue) and secondary pulse (red). Both spectra are normalized to unity. A numerical time-domain filter is applied to isolate both pulses and the ≈600 fs time separation between them matches the ≈1.6 THz interference fringes in the spectrum of b). The spectral phase of the main pulse is well within $\pm 0.05\pi$ and it is slightly quadratic for the secondary pulse.

fs), intense pulse followed by a much dimmer and stretched pulse ≈600 fs after. The fact that the time separation between both pulses roughly corresponds to the interference pattern in the frequency domain hints that both pulses have a slightly overlapping frequency content. To make sure of it, both pulses are separately filtered in time and Fourier transformed to reveal their respective spectrum and spectral phase, as shown on figure 3.1d. Both spectra

are normalized to unity for visibility; they don't contain the same amount of energy. It also highlights the overlap of two well-behaved spectra, yielding an oscillating global spectrum in figure 3.1b. As for the spectral phase, it seems to be oscillating for the spectrum coming from the main pulse, but the phase excursions are small and made of high orders of dispersion that would be hard to compress better. This leads to the quasi-FTL main pulse of figure 3.1c. For the spectral phase of the secondary pulse, there is evidently GDD (hence the longer and dimmer pulse) and would be compressible only if it was not in the same spectral region as of the one of the main pulse. Instead of traditional optical filtering or dispersion compensation techniques, cross-polarized wave generation would be an effective way of time-domain filtering by relying on nonlinear processes to suppress the least intense pulse [56]. The remaining one would be easier to compress at the cost of a reduced bandwidth.

Linking back to the measured FROG trace, we may now conclude that the main feature centered at 380 THz is the SFG of the main pulse with itself centered at 190 THz. Similarly, the small feature at 387 THz is the SFG of the secondary pulse with itself, which has a center frequency around 193.5 THz. Finally, The peaks at $\pm$600 fs are the result of the main and secondary pulses that produced SFG between 190 THz and 193.5 THz, which corresponds to the measured 383.5 THz.

The same measurement and analysis are done on the Slave laser and lead to similar conclusions since they were designed to be identical, up to their repetition rate. The equivalent of figure 3.1 for the Slave laser is presented in appendix A.

## 3.2 Stability of Repetition Rates

For DFC measurements, it is crucial that the repetition rate of both combs is stable over the entire measurement time. Otherwise, the time separation between the sequential IGMs varies and the time separation between the adjacent pulses would not increase linearly. In the frequency domain, repetition rate drifts lead to different longitudinal modes and directly affect the measured RF beats.

We use a fast photodiode (Thorlabs DX20AF) and a frequency counter (BNC Model 1105) to monitor the repetition rate of both combs over time as shown on figure 3.2a for the Master laser and 3.2b for the Slave laser. From this measurement, we see that the repetition rate variations stay within a few tens of Hz from the mean value. However, it is computed for the entire measurement time of $\approx$1.75 hours were slow drifts are also observed. The orange curves are the local variation around the mean and highlight the slow fluctuations of the repetition rates. They are obtained by applying a numerical low-pass filter and are easier to compare

with the green and red curves, which are respectively the temperature and relative humidity recorded next to the lasers by a Thorlabs TSP01 probe. Interestingly, their variations seem to roughly follow the slow ones of the repetition rate. The rise of temperature (and drop in humidity) happen after a repetition rate decrease and we attribute this sequence of events to the laser increasing the temperature inside the cavity to compensate larger decreases of its repetition rate and not the other way around. Since the probe is next to the laser heads, it is able to record this effect.

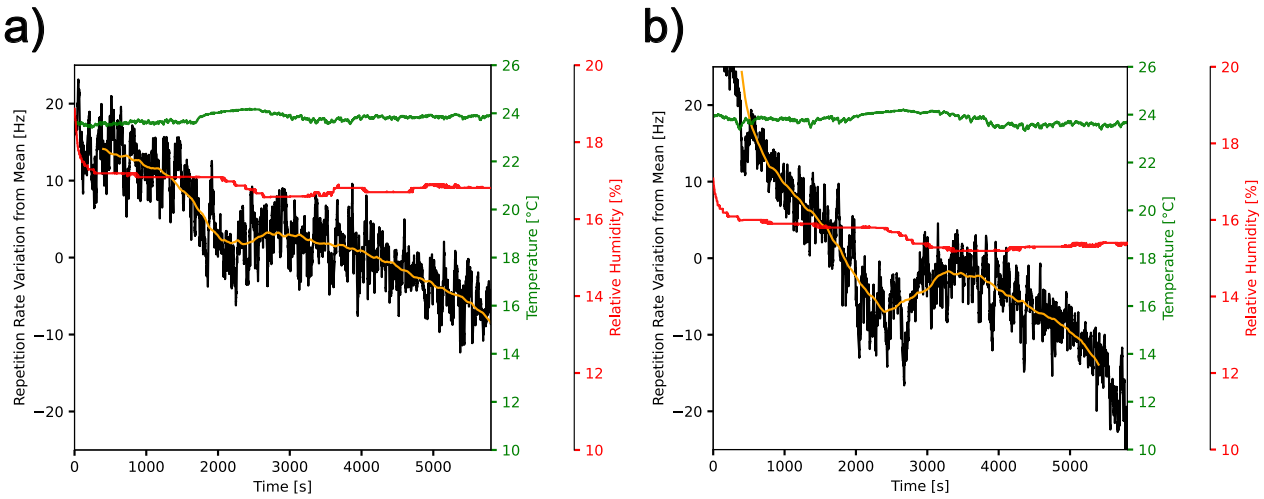


Figure 3.2 Repetition rate variations around the mean (black) for the a) Master laser and b) Slave laser for a measurement time of ≈1.75 hour where each point is separated by 100 ms. Neither measurement is recorded simultaneously and the combs are not stabilized against each other. The mean repetition rate of the Master is 99.999529 MHz and 100.001545 MHz for the Slave and the orange curves represent the local variation about the mean. The green and red curves respectively show the temperature and relative humidity level measured next to the lasers.

On shorter time-scales of a couple hundred of seconds, the repetition rates fluctuate at higher frequencies, but remain within ≈10 Hz of a local value. An FFT reveals that the faster components of the recorded signal are comprised between 3.5 and 8 mHz, which correspond to time-scales of 2 to 6 minutes. This is expected as the laser is actively adjusting the temperature in the cavity. In our case, DFC measurements are shorter than a second, so variations of the repetition rates are expected to be negligible compared to 10 Hz over minutes.

## 3.3 Stability of $f_{ceo}$

Contrarily to the repetition rate, the carrier envelope-offset frequency $f_{ceo}$ of neither comb is stabilized. It is instructive to characterize its mean and variations via $f$-to-$2f$ interferometry

as both of them play a role in DFC spectroscopic measurements. Even if both are perfectly stable in time, they may shift the measured RF spectrum towards the edges of the measurable bandwidth and unstabilized $f_{ceo}$s possibly lead to a time-dependent shift of the spectrum.

To measure $f_{ceo}$, we use a commercially available COSMO (Comb Offset Stabilization Module) $f$-to-2$f$ designed by Octave Photonics. It requires compressed pulses with energies between 150 pJ and 1000 pJ to be able to generate supercontinuum and at the same time, avoid damaging the equipment. The central frequency of the input spectrum must be near 1560 nm to output an electrical signal containing $f_{ceo}$ information from the interference of the frequency-doubled region of an octave-spanning spectrum with its fundamental. This is achieved with nanophotonic waveguide technology which enables $f_{ceo}$ characterization of low pulse-energy sources at high SNR. Although we do not actively stabilize $f_{ceo}$ in our combs, the COSMO is also ideal inside a PLL to provide a real-time measurement to stabilization electronics [57].

As detailed in section 3.1, our sources are compressed and have a central frequency around 1570 nm, which removes any broadening, filtering or dispersion compensation steps. We thus use a broadband 3 dB fiber attenuator to decrease the power of the main output down to ≈44 mW and meet the energy per pulse requirement set by the device. The COSMO is connected to the laser after it is powered on and has reached its steady state to avoid potential high optical powers upon start-ups. The input port of the COSMO is a portion of PM1550 fiber and its length can be used to compress the input pulses. In our case, a default length of 30 cm is chosen as it adds a non-significant amount of dispersion and makes it easier to manufacture and link to the lasers. The RF electrical signal resulting from the $f$-to-2$f$ optical beat is output and sampled at a 500 MS/s rate by an ADC (AlazarTech ATS9350) and its representation in the frequency domain for both combs is shown in figure 3.3a.

On figure 3.3a, a strong peak appears around 100 MHz and is attributed to the repetition rate of both lasers. In principle, it should appear as two separate peaks since they don't have the exact same repetition rate and the measurement for both combs is made separately. Many other beats are visible, but only the ones marked by a black dot are the result of a non-zero $f_{ceo}$. The remaining ones are attributed to noise and often appear in both measurements even if the $f_{ceo}$ is different for both lasers. For each of them, two beats are detected below $f_{rep}$: one is $f_{ceo}$ and the second is its complementary beat at $f_{rep} - f_{ceo}$. The opposite is plausible as well, since it is impossible to tell which one is the complementary beat. Here, $f_{ceo}$ is chosen to be the beat below $f_{rep}/2$ and is 14.652 MHz for the Master and 24.875 MHz for the Slave. Beats above $f_{rep}$ are also detected and are produced when non-adjacent modes interfere in the $f$-to-2$f$ interferometer. The sampling rate used is sufficient to resolve frequencies up to 250

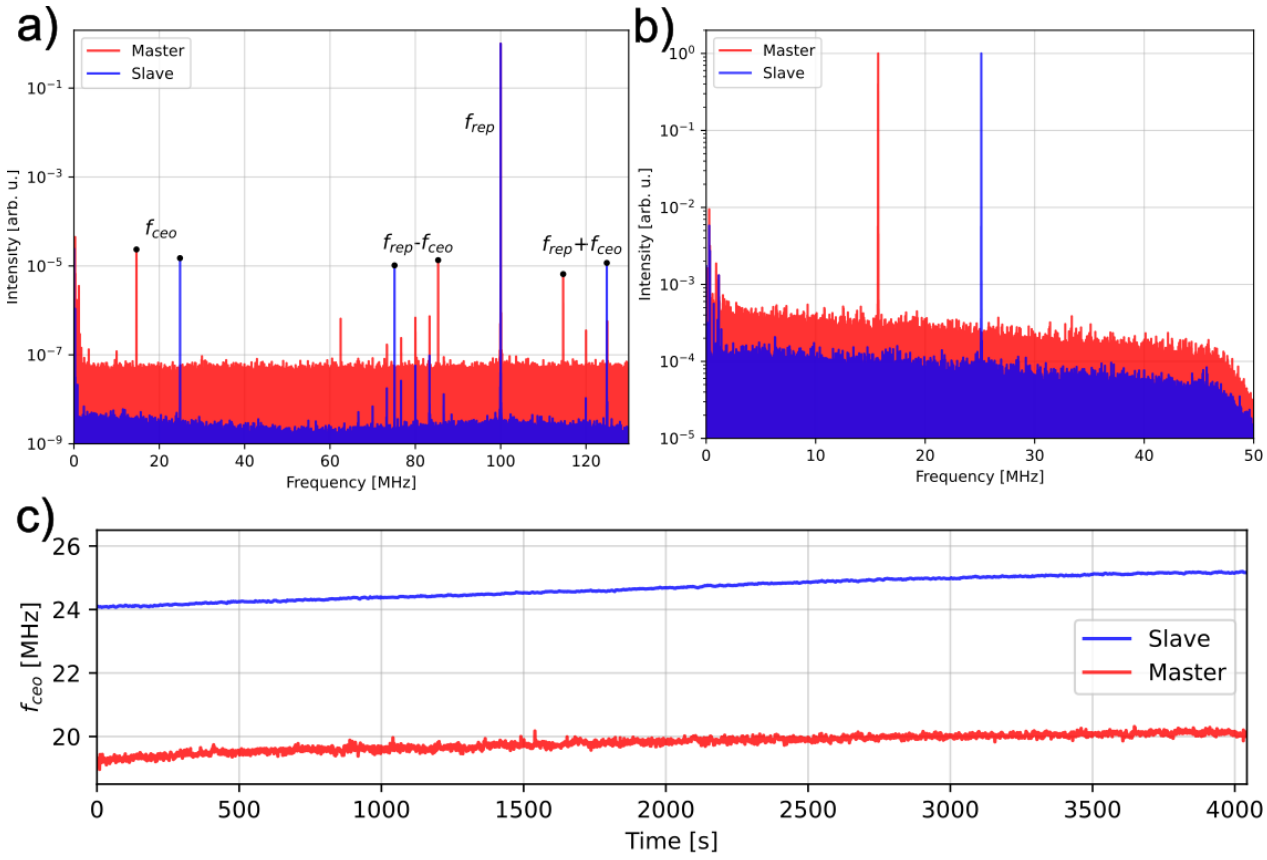


Figure 3.3 a) Unfiltered and normalized $f$-to-$2f$ spectrum for the Master (red) and Slave (blue) combs on a vertical logarithmic scale. The black dots indicate the beats that are due to a non-zero $f_{ceo}$, while the other peaks are attributed to measurement noise (except for the $f_{rep}$ peak). The signal is sampled at a 500 MS/s rate and frequencies between 130 and 250 MHz are hidden to focus on the relevant beats. b) Filtered and amplified $f$-to-$2f$ spectra. c) Time stability of $f_{ceo}$ for both combs. Measurements for c) were made on a different day, hence the notable difference in $f_{ceo}$.

MHz, but figure 3.3a only displays the first meaningful beats. Also, they are progressively less intense because the 3 dB bandwidth of the integrated photodiode of the device is 100 MHz. These beats are redundant since they reveal no new information and their position may change in time if the repetition rate is drifting. Another notable aspect of figure 3.3a is the difference in the noise floor between both measurements when normalizing to the $f_{rep}$ peak. The difference in SNR is roughly of one order of magnitude and appears to be constant over the full detection bandwidth. The main reason is the fiber-to-fiber coupling connection that was not as reliable for the Master laser than it was with the Slave laser and resulted in fewer signal for all detectable beats.

To characterize the $f_{ceo}$ stability of both frequency combs, we isolate the lowest frequency

beat via a combination of low-pass and high-pass analog filters. Additionally, the remaining electrical signal is amplified by two low-noise RF amplifiers (Mini-Circuits ZFL-1000LN+) in series to improve the peak-to-peak voltage from a couple of mV to 200 mV, the minimal voltage threshold for stability measurement with our frequency counter. The signal is not amplified any further since noise is also amplified in a non-negligible manner. Another limitation is that only one power supply is used for both amplifiers, which provides a single tunable gain parameter: the output of the first amplifier needs to be below the damage threshold of the input of the second amplifier.

The result of the filtering and amplifying procedure is shown in the frequency domain on figure 3.3b for both combs. As intended, the $f_{ceo}$ peaks are now the most intense features even if their SNR are not necessarily better. Again, the noise floor in the case of the Master laser is more important since it requires more amplifying to compensate for a dimmer $f_{ceo}$ signal which adds more noise over the entire detection bandwidth. The sudden decrease of spectral intensity around 50 MHz is caused by the low-pass filters used to discard complementary and non-adjacent beats and the repetition rates. Compared to the $f_{ceo}$ peaks in figure 3.3a, the ones in 3.3b are slightly displaced even if both measurements are made one after the other. This is an example of how the unstabilized $f_{ceo}$ of a frequency comb can shift after only a few minutes.

To capture slower $f_{ceo}$ drifts over time, we send the signal plotted in 3.3b to our frequency counter and measure it for a duration of around one hour. The result is shown on figure 3.3c where we can see a linear $f_{ceo}$ drift of 1 to 1.5 MHz for both combs. The mean value for each of them is different from what is presented on figures 3.3a and b since our system is not designed to maintain a specific $f_{ceo}$ value from day to day. At least, we observe that the drifts around a local mean value are slowly varying. The red signal (Master laser) seems to be noisier than the one obtained with the Slave laser (blue spectrum) and we attribute these variations to the problematic fiber-to-fiber connection and the amplification of noise around the value of $f_{ceo}$.

### 3.4 Stability of the Repetition Rate Difference

The timing of our DFC system is based on the Master laser, which has a non-tunable repetition rate that may drift in time even with active thermal stabilization, as shown in section 3.2. To ensure coherence with the Master comb, the repetition rate of the Slave comb is also stabilized thermally, but features a PZT to rapidly correct for fluctuations of the Master's repetition rate. Put differently, our system is mutually coherent as we do not ensure that the individual repetition rates are absolutely fixed in time and only stabilize the detuning such

that the repetition rate fluctuations of the Master are transmitted to the Slave laser. This is achieved via a PLL shown on Figure 3.4.

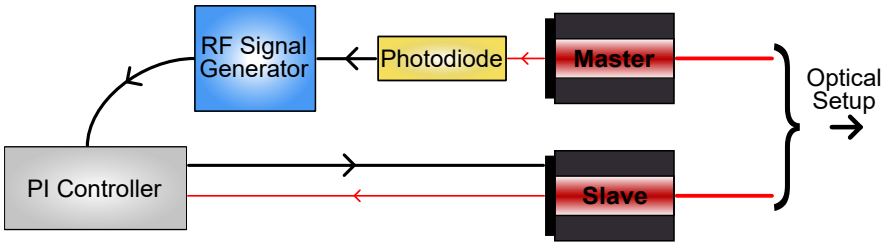


Figure 3.4 Schematic of the PLL built to ensure mutual coherence between the two frequency combs. Red lines indicate optical signals and black ones are for electrical signals. A 2 mW tap from the Master is sent to a fast photodiode to generate an electrical signal that acts as a reference input to a RF signal generator. It outputs a CW signal at a frequency corresponding to the 30th harmonic of the desired repetition rate of the Slave laser to the PI controller. The Slave's secondary output is also sent to the PI controller, which compares and adjusts the repetition rate to match it to the desired input.

The secondary output of the Master is converted to an electrical signal by a fast photodiode (Thorlabs DX20AF). Its 3 dB bandwidth extends to 20 GHz so the arrival time of individual pulses is well resolved. This pulsed signal acts as a clock for the whole system as it captures repetition rate variations of the Master. At this stage, the output of the photodiode provides sufficient information to actively stabilize the Slave's repetition rate to a specific value with a Proportional-Integral (PI) controller and stabilization electronics. In practice, our PI controller (NKT Photonics Ultra Low-Noise Synchronization Module) requires a reference corresponding to the 30th harmonic of the desired Slave's repetition rate. This is achieved via a tunable Microwave/RF signal generator (BNC Model 845) that generates a CW Slave reference signal yielding detunings of $0 \leq \delta f_{rep} \leq 8$ kHz. Since it is more important to maintain a fixed repetition rate difference rather than a fixed Slave repetition rate, the Master signal is fed to the reference input port of the RF generator. Such generators usually have a precise and stable internal reference, but here we intentionally bypass it to be sensitive to any variations of the repetition rate of the Master laser. The PI controller compares the 30th harmonic of the Slave's repetition rate through its secondary optical output with the output of the RF generator and adjusts the repetition rate of the Slave comb via the PZT in its cavity so both inputs match.

The best way to quantify the stability of the detuning while using the PLL in figure 3.4 would be to measure both repetition rates in (or out) of the loop with separate photodiodes and frequency counters to monitor the difference. However, only one frequency counter was available for this project and it is only able to record one channel or frequency ratio at a time.

Recording the repetition rate of either comb does not reveal new information and directly measuring the time separation between the IGMs requires the optical experimental setup discussed below in section 4.1. Instead, we measure $R = 30(f_{rep} + \delta f_{rep})/f_{rep}$, the frequency ratio between the 30th harmonic of the Slave laser repetition rate as outputted by the PI controller and the Master repetition rate from its reference signal to infer the stability of $\delta f_{rep}$. Of course, this measurement contains drifts of both $f_{rep}$ and $\delta f_{rep}$ and it is impossible to tell the contributions apart with a single measurement. Characterization steps described in section 3.2 hint that $f_{rep}$ drifts are small especially on short time scales so we make a separate $f_{rep}(t)$ stability measurement immediately after measuring $R$ to replicate environmental fluctuations to the best of our capability. Doing so, fluctuations of the repetition rate difference can be characterized with

$$\delta f_{rep}(t) = \langle \delta f_{rep}(t) \rangle + \Delta(\delta f_{rep}(t)) = f_{rep}(t)\left(\frac{R(t)}{30} - 1\right) \tag{3.1}$$

by removing the mean detuning from the time-varying $\delta f_{rep}$. Figure 3.5 shows the effect of the reference type on the fluctuations of the detuning around its mean using equation 3.1.

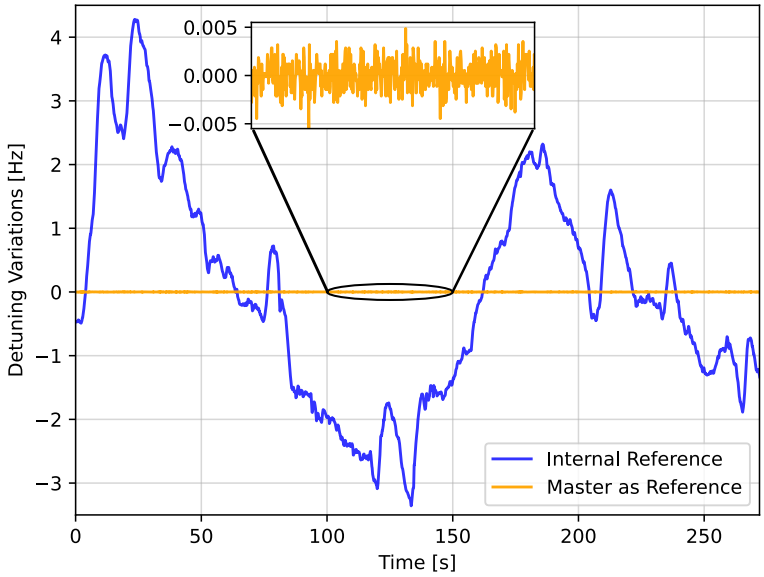


Figure 3.5 Repetition rate difference variations around its mean when the Master laser is used as a reference (orange) and when the internal reference of the RF generator is used instead (blue). The separate repetition rate stability measurement reveals $f_{rep}$ =99.999721 MHz with a standard deviation of 951 mHz. The mean detuning is 210.64 Hz with the Master as reference and 208.85 Hz without. The point spacing is 100 ms and the acquisition time is about 5 minutes. The inset shows how smaller the detuning fluctuations are when the Master comb is the reference for the DFC system.

With figure 3.5, we can clearly see that it is advantageous to use the Master as the reference to minimize $\delta f_{rep}$ fluctuations as the same $f_{rep}(t)$ stability measurement is used for both reference types. Fluctuation differences around $\langle \delta f_{rep}(t) \rangle$ are thus due to different fluctuations in $R(t)$. With the internal reference, the observed drifts often span past $\pm 1$ Hz and approximately correspond to 1% of the mean detuning. The variations about the mean present a similar signature to the one of the repetition rate of a single comb which hints that the repetition rate of the Slave laser is stabilized very well by the PLL and that drifts of the repetition rate of the Master are recorded through the measurement of $R(t)$. On the other hand, the inset of figure 3.5 shows that using the Master comb as a reference for the whole system maintains detuning drifts below $\pm 5$ mHz which corresponds to a relative drift of $\approx$0.005%. Detuning fluctuations are thus 3 to 4 orders of magnitude smaller with the Master as reference than with the internal reference of the RF generator.

Even if detuning fluctuations cannot be exactly characterized, measuring the $R$ ratio provides an idea of the time-varying compression factor $m(t)$. Using its definition in equation 2.14, the maximal number of detected RF modes $m(t)/2$ as a function of $R(t)$ is

$$\frac{m(t)}{2} = \frac{1}{2}\left(\frac{1}{\frac{R(t)}{30} - 1} + 1\right), \tag{3.2}$$

which relies on a single measurement. The standard deviation of $m(t)/2$ is 1947 RF modes with the internal reference and 1.72 with the Master as reference. By multiplying both of these by their respective mean detuning, we get the additional (or subtracted) RF bandwidth due to detuning fluctuations if the full available optical bandwidth is occupied: 406 kHz and 363 Hz respectively. Moreover, to convert the RF spectrum to optical frequencies, an additional $m$ factor is required so the error on the RF bandwidth is multiplied. For precision spectroscopy applications, it is crucial that the spectra retrieved from the sequential IGMs contain the same information, especially with coherent averaging. Averaging spectra with different central frequencies and bandwidths may result in a spectrum with washed-out features and inexact information. To avoid these issues, we use the Master laser as the reference for the DFC system and minimize jitters in the IGMs' arrival time.

# CHAPTER 4 EXPERIMENTAL SETUP

With both frequency combs characterized and an efficient PLL to enforce mutual coherence between them, the main goal of this project is to do DFC spectroscopic measurements of a known gaseous acetylene sample and retrieve its expected absorption and dispersion signature to prove the setup is performing well. The optics and geometry of the setup using balanced detection through polarization mixing are first explained followed by a calculation that justified the introduction of nonlinear fibers to broaden the initial spectrum of both combs.

## 4.1 Optical Setup

As described in sections 2.2.2 and 2.2.3, DFC interferometers rely on the interference of two slightly detuned frequency combs where the RF beats are measured by sampling a train of IGMs. Experimentally, combining two sources of similar spectrum in a co-linear way can be achieved via BSs that act as beam combiners in this case. Standard BSs may be used by sending one laser per input port and both combs will interfere in both exit ports of the BS, which is ideal to perform Balanced Detection (BD) [1]. While this method is simple and cheap, it requires identical optical filtering on both branches to meet the Nyquist sampling condition set by the DFC method. Even with two identical filters, slight differences in their transmission properties may affect the measured beats. Moreover, BD usually calls for near-identical powers incoming on both photodetectors and relying on standard BSs means both branches must be separately attenuated with Neutral Density (ND) filters to reach equal intensities.

For these reasons, we choose a different setup geometry inspired by [33], where a Polarizing Beam-Splitter (PBS) replaces the normal BS and HWPs are added in a way to create a single light-path before BD. This section in the optical setup is particularly useful to apply identical optical filtering and attenuation on both combs. The filtering step is not mandatory if the detuning between both combs is small enough such that their overlapping bandwidth meets the Nyquist condition. To enable greater detunings, narrow-bandwidth optical filters such as Thorlabs FBH1530-12 or Semrock NIR01-1550/3-25 are used to keep wavelengths near the absorption features of our acetylene sample or keep an even narrower spectrum.

Figure 4.1 shows our version of the complete spectroscopy setup where both combs can first be broadened via a section of HNF (further detailed in section 4.4). The broadening step is

optional as is it only relevant for the spectroscopy of the acetylene sample; each HNF section is connected to a pair of collimators (Thorlabs TC18FC-1550) to facilitate the alignment of their input and yield a collimated output. The collimators are easily removable from their mount to rapidly shift to the unbroadened combs.

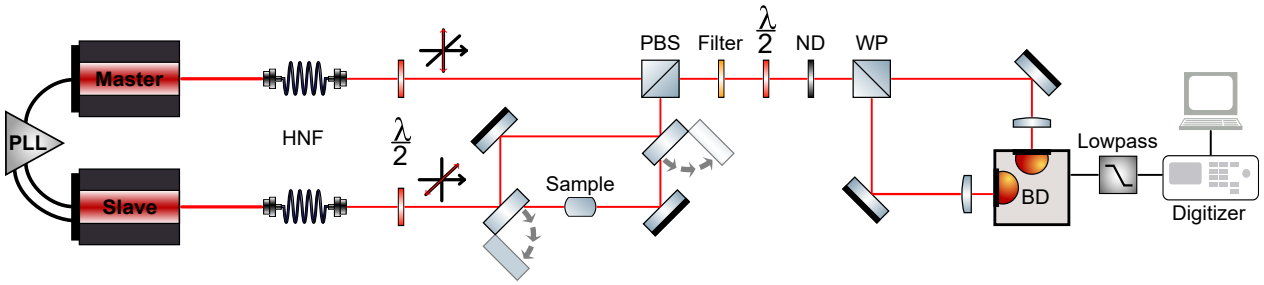


Figure 4.1 Optical setup used to perform DFC spectroscopy of an acetylene sample. The spectrum of both frequency combs is optionally broadened by ≈10 cm of HNF and two HWPs set the polarizations orthogonally. A set of removable mirrors controls the path of the Slave frequency comb. They are combined at the PBS and optically filtered to meet the Nyquist sampling condition. Another HWP rotates the polarizations to diagonal and anti-diagonal and a Wollaston Prism (WP) splits horizontal and vertical polarizations. Both outputs are focused on each port of a balanced detector. The BD signal is analogically low-pass filtered at $f_r/2$ and digitized.

## 4.2 Balanced Detection

To generate a BD signal, an HWP (Thorlabs WPH05M-1550) is placed in the path of each comb to set their polarization aligned with the polarization input ports of a PBS (Thorlabs PBS204): one vertically and the other one horizontally. Doing so, very little power losses are measured in the remaining port of the PBS and may be attributed to the quality of the PBS, HWPs and polarization extinction ratio of the original sources. The function of the PBS is to combine both lasers, but they do not interfere since they are in orthogonal polarizations. In order to generate RF beats, a third HWP is introduced after both combs are spatially combined and its fast axis is set at a 22.5 ° angle from the vertical axis to shift the polarization of both sources by 45 ° and yield diagonal and anti-diagonal polarizations. Mathematically, the polarization states of the combs after the final HWP can be described in the following way:

$$E_M(t) : \frac{1}{\sqrt{2}}\big(H + V\big), \qquad E_S(t) : \frac{1}{\sqrt{2}}\big(H - V\big), \tag{4.1}$$

where $E_M(t)$ and $E_S(t)$ refer to the time-dependent electric field of the Master and Slave comb, respectively. A Wollaston Prism (WP) (OptoSigma WPPB-10-18SN) is then used to project those new polarization states on its horizontal ($H$) and vertical ($V$) axes and produce two outputs ready for both ports of the balanced detector (Femto HBPR-200M-30K-IN-FST). The WP effectively acts as a two-channel polarization filter such that both output ports contain a combination of the electric field of both combs:

$$E_H(t) : \frac{1}{\sqrt{2}}\Big(E_M(t) + E_S(t)\Big), \qquad E_V(t) : \frac{1}{\sqrt{2}}\Big(E_M(t) - E_S(t)\Big). \tag{4.2}$$

The time-dependent intensity of both signals is measured by separate photodiodes:

$$I_H(t) = E_H^* E_H = \frac{1}{2}\Big(I_M + I_S + E_M^* E_S + E_S^* E_M\Big), \tag{4.3}$$

$$I_V(t) = E_V^* E_V = \frac{1}{2}\Big(I_M + I_S - E_M^* E_S - E_S^* E_M\Big). \tag{4.4}$$

Up to their Common-Mode Rejection Ratio (CMRR), balanced detectors subtract both measured intensity signals to yield a DC-free BD signal $S_{BD}(t)$ [33]:

$$S_{BD}(t) = I_H(t) - I_V(t) = 2\mathrm{Re}(E_M^* E_S). \tag{4.5}$$

Considering that both combs have an electric field of the same form as equation 2.3 with a non-zero $f_{ceo}$, the BD signal becomes

$$S_{BD}(t) = 2\mathrm{Re}\bigg(\sum_n \sum_p A_{M,n} A_{S,p} \exp\Big((f_{rep}(p-n) + p\delta f_{rep} + \Delta f_{ceo}) i 2\pi t + i\Delta\phi_{pn}\Big)\bigg), \tag{4.6}$$

where $A_{M,n}$ and $A_{S,p}$ are respectively the amplitude of the mode $n$ of the Master comb and mode $p$ of the Slave comb and $\Delta f_{ceo} = f_{ceo,S} - f_{ceo,M}$ and $\Delta\phi_{pn} = \phi_{S,p} - \phi_{M,n}$. In the case where the optical filter in figure 4.1 has a bandwidth that is well suited for the incoming repetitions rates (equation 2.17) and that $p = n$, equation 4.6 represents nothing else than an RF comb of beat frequencies $\nu_{n,RF} = n\delta f_{rep} + \Delta f_{ceo}$ with amplitudes $A_{n,RF} = A_{M,n} A_{S,n}$ and spectral phase $\Delta\phi_{nn}$. Since the free-spectral range of the RF comb is the detuning between both optical combs, the period of this periodic signal is $1/\delta f_{rep}$ and its real part is measured

by the balanced detector. The $p \neq n$ case represents complementary or non-adjacent beats above $f_{rep}/2$; low-pass analog filters (Mini-Circuits BLP-44+ and SLP-50+) between the balanced detector and the ADC in figure 4.1 suppress them to yield

$$S_{BD}(t) = 2\sum_n A_{n,RF}\cos\Big(2\pi\nu_{n,RF}t + \Delta\phi_{nn}\Big). \tag{4.7}$$

Characterization of $f_{ceo}$ in section 3.3 showed that $\Delta f_{ceo}$ could reach values of few MHz, but by definition, the actual RF carrier-envelope offset frequency $f_{ceo,RF}$ must be smaller than $\delta f_{rep}$. In this case, a large $\Delta f_{ceo}$ results in a shift of the RF spectrum and if $f_{rep}$ is a multiple of $\delta f_{rep}$, the real $f_{ceo,RF}$ is $\mathrm{mod}_{\delta f_{rep}}(\Delta f_{ceo})$. If $\Delta f_{ceo} = k\delta f_{rep}$, but the nominal repetition rate is not a harmonic of the detuning, a non-zero $f_{ceo,RF}$ may still be observed. In all cases, the presence of a non-zero $f_{ceo,RF}$ can be seen as a mismatch between phase and group velocities of the components of the IGMs, in similar fashion than with optical pulses.

The RF comb also has a spectral phase term $\Delta\phi_{nn}$ which is the result of the subtraction of the spectral phases of the optical combs. If they are not identical, the resulting spectral phase directly affects the shape of $S_{BD}(t)$: constant and linear terms respectively apply a phase and rigid shift to the whole signal, where quadratic terms apply chirp, etc. Having access to the dispersion of the RF comb itself is not particularly relevant, but it means the dispersion of a sample $\Phi_n$ can be measured if it is placed in front of a single comb, as in figure 4.1. Transmission features $T_n$ are also imprinted in the measured signal and modify equation 4.7 in the following way:

$$S_{BD,sample}(t) = 2\sum_n T_n A_{n,RF}\cos\Big(2\pi\nu_{n,RF}t + \Phi_n + \Delta\phi_{nn}\Big). \tag{4.8}$$

The signature of the sample is then retrieved by comparing the Fourier transform of equation 4.8 with the one of equation 4.7:

$$T_n = |R_{sample}|, \qquad \Phi_n = \arctan\left(\frac{\mathrm{Im}(R_{sample})}{\mathrm{Re}(R_{sample}}\right), \tag{4.9}$$

where the response function of the sample $R_{sample}$ is defined as

$$R_{sample} = \frac{\mathcal{F}(S_{BD,sample})}{\mathcal{F}(S_{BD})}, \tag{4.10}$$

where $\mathcal{F}$ denotes a Fourier transform. Since the absorption and dispersion of the sample

are retrieved regardless of the ones added by the optics in the setup during the reference measurement, additional dispersive optics can be added to stretch one of the BD inputs and avoid detector saturation with greater optical powers [44].

## 4.3 Sampling the IGMs

The signal measured by the BD is analog and is converted to a digital signal representing the sequence of IGMs by our ADC. With the detectable RF bandwidth being from DC to $f_{rep}/2$, the variable sampling rate is chosen to be between 100 and 500 MS/s. The $\delta f_{rep}$ detuning is tuned to yield an RF spectrum that goes to near-zero intensity at the edges of the available bandwidth. According to the Nyquist theorem, this scenario still calls for a sampling rate of at least 100 MS/s to resolve the fastest components. The fastest sampling rate of the acquisition card is 500 MS/s and is useful to better resolve the arrival time and CEP of individual IGMs for the data-correction algorithm detailed in section 5.3.1. On the downside, larger data files and computing times result from this oversampling.

## 4.4 Self-Phase Modulation Broadening

We broaden the spectrum of both combs through Self-Phase Modulation (SPM) with a short section of HNF (Thorlabs HN1550P) to have a better overlap with the absorption features of our acetylene cell. The fiber assemblies are home-made and composed of bare fiber and two FC/PC connectors to easily link to collimators. Their experimental output is compared to the simulated ones with pyNLO, a Python library modelling pulse propagation in nonlinear media [58].

### 4.4.1 Self-Phase Modulation

In order to benefit from SPM, the pulse must go through a nonlinear medium that has an intensity-dependent refractive index $n_{NL}$ [22]:

$$n_{NL}(I) = n_g + n_2 I(t), \tag{4.11}$$

where $n_g$ is the linear wavelength-dependent refractive index, $n_2$ is the nonlinear refractive index and $I(t)$ is the time-dependent intensity profile of the pulse. The acquired phase shift by propagation through the nonlinear medium with respect to the linear part is

$$\Delta\phi(t) = \frac{2\pi\nu_0 n_2 I(t) L}{c}, \tag{4.12}$$

where $L$ is the length of the medium. The *instantaneous frequency* shift is the derivative of the phase shift:

$$\Delta\omega(t) = \frac{2\pi\nu_0 n_2 L}{c}\frac{\partial}{\partial t}I(t). \tag{4.13}$$

Equation 4.13 means new frequencies are generated if the incoming pulse is intense and compressed enough. In the case of HNFs, a nonlinear coefficient $\gamma$ is commonly defined as

$$\gamma = \frac{2\pi c}{\nu_0}\frac{n_2}{A_{eff}} \tag{4.14}$$

to take into account the area of the effective mode size $A_{eff}$ at the central frequency $\nu_0$ and appears in the nonlinear Schrödinger equation [59].

### 4.4.2 Simulations with pyNLO

With compressed pulses of 1 nJ, preliminary simulations revealed only few (≈5) centimeters would be required to reach an appreciable broadening. However, a minimal length of ≈10 cm is set by a combination of the length of the connectors and our assembling and polishing capabilities. Doubling the fiber length for such energy per pulse may broaden the spectra even more than what is needed and would result in less optical power in the relevant spectral region. In our case, coupling losses between the collimators and fibers tend to significantly decrease the incoming average power in a way to *cancel* the effects of a longer fiber.

Simulations with the pyNLO Python package are made to estimate the SPM output spectra for different realistic input pulse energies and confirm that they overlap with the 196 THz absorption features of acetylene. To generate the numerical input pulse, the FWHM pulse duration of the main retrieved pulse in section 3.1 is used alongside its central frequency. We assume the contributions of the secondary pulses to nonlinear effects are negligible due to their low intensities and the GDD of the main pulse is inferred from equation 2.8 where $\tau_0$ is the FTL pulse duration. The real sign of GDD is unknown for the simulations and they are done for both cases; the resulting spectra are similar for such short fibers and low pulse energies. TOD effects are neglected and the bandwidth of the Gaussian spectrum is deduced from the FTL duration. The repetition rate of the sources is approximated to 100 MHz in both cases since the repetition rate is not appreciably tunable experimentally. The energy per pulse is varied between 100 pJ and 500 pJ to simulate the remaining energy per pulse due to coupling losses. The incoming pulse interacts with the fiber and its dispersion parameters need to be specified to predict the output spectrum. The interpretation of the dispersion curve of a fiber $n_g(\lambda)$ is highly analogous to the spectral phase of a pulse (equation 2.5): it indicates the additional spectral phase that is applied to the pulse after propagation. For our

simulations, the relevant dispersion parameters are its dispersion $D$ and its slope $S$ defined as

$$D = -\frac{\lambda}{c}\frac{\partial^2 n_g}{\partial \lambda}, \qquad S = \frac{\partial D}{\partial \lambda}. \tag{4.15}$$

Numerically, the fiber is generated using $D = 1$ ps/(nm·km) and its slope $S = 0.006$ ps/(nm$^2$km) at 1550 nm, attenuation and nonlinear coefficients ($\alpha = 0.9$ dB/km and $\gamma = 10.8$ W$^{-1}$km$^{-1}$ respectively) [60], and a test length of 10 cm. The input pulses are then propagated through the fiber following the Fourth-order Runge-Kutta in the Interaction Picture (RK4IP) method [61]. Figure 4.2a compares the simulated SPM spectra of the Master comb for different pulse energies with the acetylene features when assuming a positive pulse GDD.

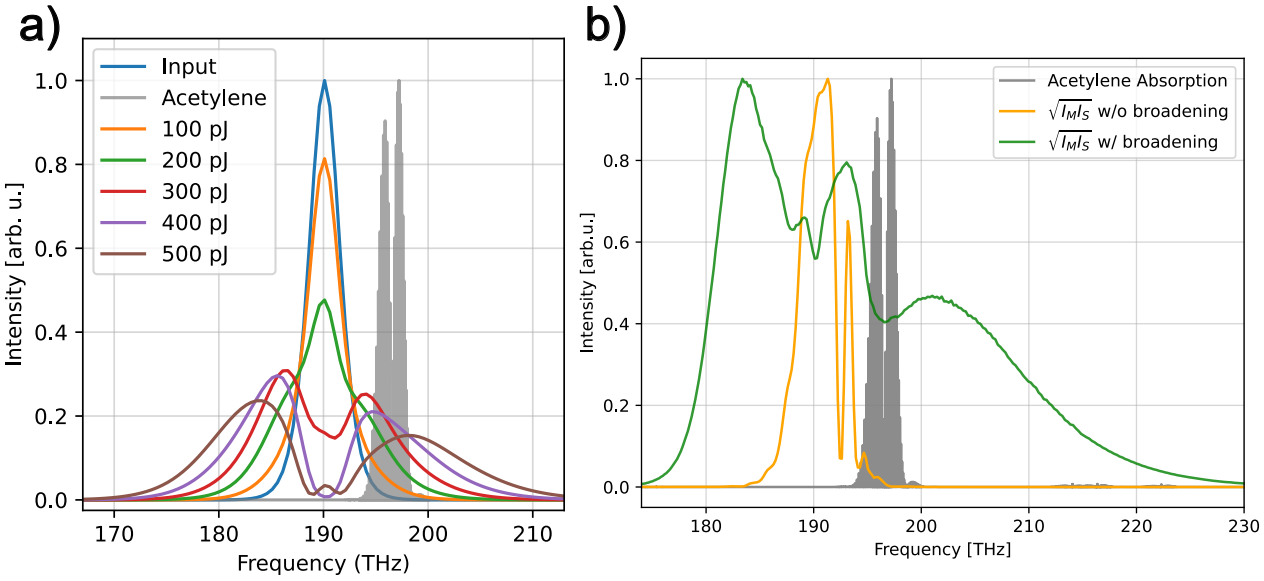


Figure 4.2 a) Simulated SPM spectra as a function of the input energy per pulse for the Master compared to the 196 THz absorption region of acetylene (grey). All SPM spectra are normalized to input spectrum (blue) so the total energy (area under the curve) is conserved between different spectra (up to losses in the fiber). b) Comparison between the un-broadened FROG-retrieved (orange) and measured broadened spectra (green) after both combs are interfered with the 196 THz absorption feature of acetylene from the HITRAN database (grey). A multiplicative factor of $\lambda^2/c$ is applied to the spectrum measured with the spectrometer when converting them from wavelengths to frequencies to preserve the total energy [5].

From the spectra of figure 4.2a, we can conclude that input pulse energies between 400 and 500 pJ are ideal to maximize the overlap with the absorption band of acetylene when using

a fiber length of 10 cm. As the input energy is increased, the expected broadening due to SPM [22] is first seen with 100 pJ and 200 pJ and a spectral splitting appears with even higher pulse energies and leads to a third dim central peak at 500 pJ. Experimentally, a combination of coupling losses in the fibers and attenuation easily reduces the original 1 pJ pulse energy to the required range. Although this broadening brings more sensitivity, important power losses are expected across the new spectrum and makes the alignment of the setup far more difficult.

### 4.4.3 Experimental SPM Spectra

Our home-made fiber assembling process is a fast and easy way to connect them to collimators, but the length of the connectors and the polishing procedures prevent us from having two short and identical fiber lengths: 12.5 cm on the Master laser branch and 14 cm for the Slave laser were the two shortest fiber sections assembled. Alignment in the collimators is easier than to focus in the few-$\mu$m core of the fiber with a lens or parabolic mirror, but comes with much more power losses. According to the simulations of section 4.4.2, the output spectrum should be broadened even more with longer fibers, but the highest measured output power is only 28 and 34 mW ($\approx$280-340 pJ pulses) in a way to potentially even out the additional broadening due to longer fibers. The pulse energy can be tuned by slightly changing the alignment in the collimators as a proof-of-principle, but a proper stretcher-compressor would be required to provide a more appropriate peak-power tunability. In the current implementation, a misalignment in the collimators inevitably lowers the output power, but may concentrate the remaining energy towards the spectral regions that are relevant to the sample. When maximizing the output power of both fibers, the SPM spectra are measured with an InGaAs grating spectrometer (Ocean Optics NirQuest+1.7) and the normalized squared root of their product is compared to its equivalent as retrieved by the FROG measurement on figure 4.2b. Even if the total energy between neither spectrum is the same, the main goal to better overlap with the acetylene NIR absorption features is achieved. However, the fibers constituted an advanced step in the project and were not used for measurements presented in chapter 5 since they reduce the available optical power and add yet another component to take into account in the characterization. Their addition in the setup opens up the door to broadband spectroscopy of samples given the large bandwidth of $\approx$35 THz only using the original pulse energies of 1 nJ.

# CHAPTER 5 RESULTS

This section presents the main DFC results of this project, starting with the procedure to extract the RF spectrum from a single IGM and convert it toward optical frequencies where it can be compared with a reference spectrum. A coherent averaging method relying on the correction of fluctuations of both degrees of freedom of the RF comb is then detailed and the SNR gain is demonstrated. Preliminary absorption and dispersion measurements of an acetylene sample are shown and compared to the HITRAN database.

## 5.1 RF Spectrum of a DFC Source

Retrieving optical information about a source or sample with DFC spectroscopy begins with a few steps of signal analysis of the periodic IGMs. They form a real signal (equation 4.7) and are sampled at a sampling rate of 500 MS/s which enables resolving frequencies between DC and 250 MHz. The expected RF spectrum should fall between DC and $f_{rep}/2$ and such a high sampling rate resolves frequencies where no signal is expected and only contribute to noise. It is set this way to facilitate the identification of the CEP and arrival time of each IGM for better correction in section 5.3.1. It is also helpful to coarsely measure the repetition rate of both combs since their RF component is strong enough to be detectable even with multiple analog low-pass filters between the detector and the ADC. At least, the measured signal can be Fourier transformed to apply a numerical band-pass filter around the relevant features to remove noise coming from DC and higher frequencies. An inverse FFT of the remaining RF spectrum provides a cleaner sequence of IGMs out of which the envelope is computed by first finding the numerical Hilbert transform of the signal [62]. Figure 5.1a shows a sequence of three IGMs separated by $\approx 10$ ms ($\delta f_{rep} = 99.7$ Hz) where a sharp numerical band-pass filter has been applied to remove noise outside the 6-20 MHz range, where the initial RF spectrum is.

As expected from a DFC (or analogously with a Michelson) interferometer, no interference signal is recorded for most delays, but a strong oscillating pattern is observed when the pulses are synchronized in time. The zero-intensity optical bandwidth of both the Master and Slave is on the order of 15 THz and the detuning of 99.7 Hz enables optical bandwidths up to $\approx 50$ THz: it is purposely made smaller than required to yield an RF spectrum far from the edges of the detection bandwidth. When zooming on one of the IGMs in figure 5.1b, we see two pairs of secondary IGMs that are respectively separated by 22 and 44 $\mu$s from the main IGM. We attribute their presence to an etalon effect [63] coming from Fresnel reflections in one

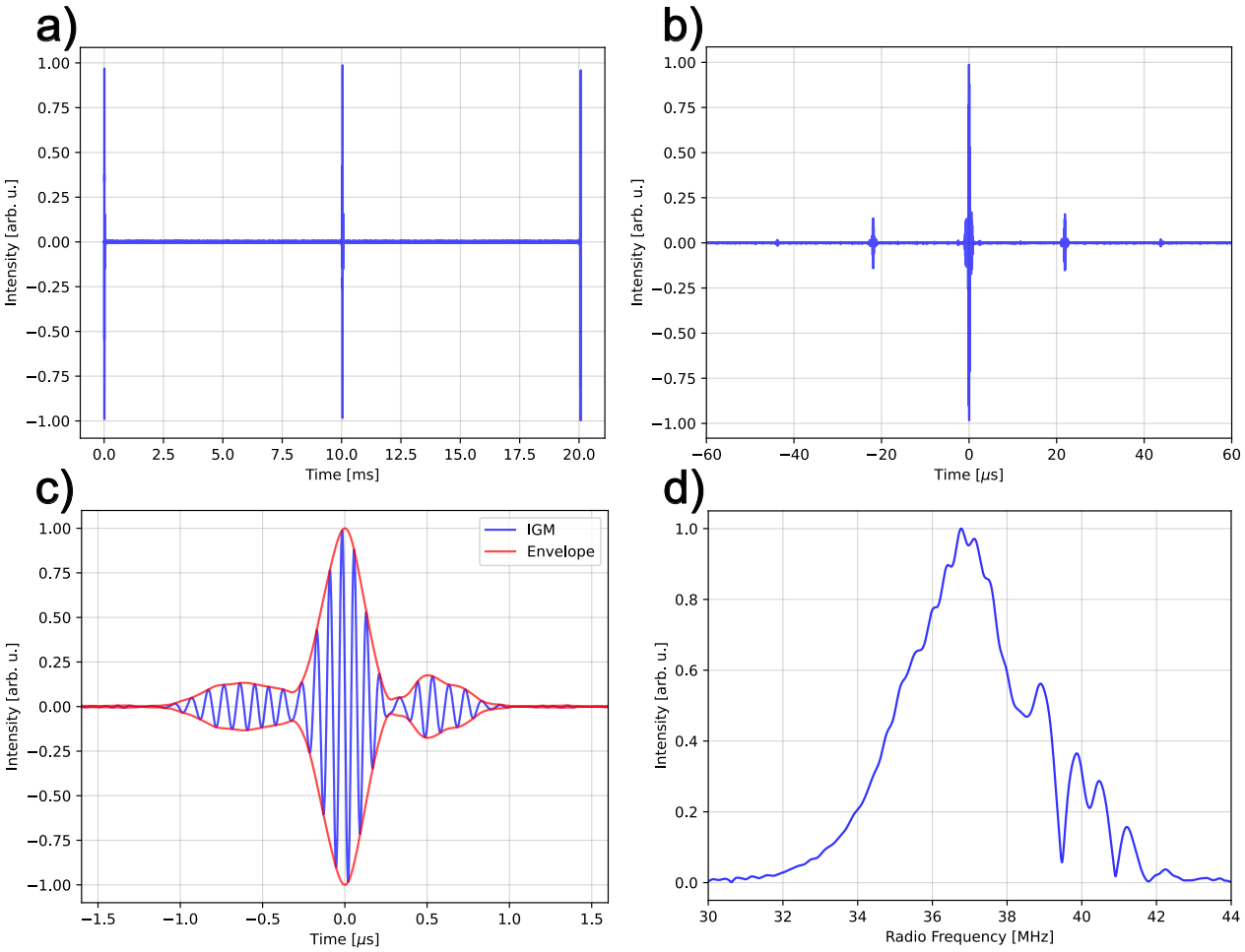


Figure 5.1 a) Sequence of three normalized and numerically filtered IGMs resulting from the interference of both unfiltered and un-broadened combs with $f_{rep}$ = 99.999442 MHz and a repetition rate detuning of 99.7 Hz where the signal is sampled at a sampling rate of 500 MS/s. b) Zoom on the IGM at 10 ms in a) (re-centered at $t = 0$) to reveal secondary IGMs due to an etalon effect. c) Zoom on the main IGM to show the expected oscillating pattern (blue) and its envelope (red). d) FFT of the IGM in c) to reveal the RF spectrum of the DFC source after inversion with respect to $f_{rep}/4$.

of the optics in the single-path region of the experimental setup. The reflections cannot be anywhere else in the setup because they would lead to secondary IGMs only on one side of the main one. Moreover, the thickness $L$ of the optic responsible for those can be estimated with $L = \frac{c}{2n_g}\frac{\Delta t}{m}$, where $\Delta t$=22 $\mu$s is the time separation between a main and closest secondary IGM, $n_g \approx 1.5$ is an approximation for the group refractive index if it's made of BK7 glass [64] and $m$ =1003140 is the compression factor which converts the laboratory times to effective times. The factor of 2 in the denominator accounts for the back and forth path in the optic; the thickness is thus on the order of 2.2 mm. One possible culprit in this section of the setup

is the 2 mm thick ND filter made of ultraviolet fused silica ($n_g \approx 1.44$ at 1.57 $\mu$m [65]). The slight discrepancy may come from the angle given to the filter to avoid back-reflections from the first interface, which increases its effective length.

Figure 5.1c focuses on the main IGM and shows the measured oscillating signal that has a central frequency of a few MHz. The envelope is shown in red and highlights the non-zero CEP of the IGM resulting from a non-zero $f_{ceo,RF}$ and/or its fluctuations. In fact, the parasitic IGMs of figure 5.1b are not concerning as each (main) IGM is isolated from the other ones and a boxcar (or time-domain band-pass) filter is applied to remove noise at frequencies that are not discarded by the frequency-domain band-pass filter mentioned above. Here, the boxcar filter is 7 $\mu$s wide to keep a small feature (not shown) at $\pm 3$ $\mu$s and centered with the peak of the envelope of the IGM.

The FFT of a time-filtered IGM should yield a noise-free RF spectrum that could be converted to optical frequencies, but there is a potential spectral inversion with respect to $f_{rep}/4$ as discussed in section 2.2.3. For this measurement, the central optical frequency is around 191 THz and the maximum optical bandwidth for the repetition rates involved is 50.16 THz. Thus, the integer division $\lfloor \nu_0/\Delta\nu_{max} \rfloor = 3$, which means an inversion of the RF spectrum is required to appropriately represent the optical spectrum of the DFC source. For this calculation, the required precision on the central optical frequency depends of $\Delta\nu_{max}$: the greater it is, the coarser the precision on $\nu_0$ can be. For example, if $\Delta\nu_{max}$ is 1 THz, an inexact central frequency on the order of 1 THz is sufficient to change the result of the integer division. Of course, a separate reference measurement is necessary to identify the central frequency, and can be done with a spectrometer.

Figure 5.1d shows the RF spectrum corresponding to a single IGM after being inverted and we can see that its intensity goes to zero at 30 and 44 MHz which represent the edges of the 6-20 MHz band-pass filter after inversion. The signature of the boxcar filter is also notable on the inverted RF spectrum as it removes any oscillation faster than $1/(7\ \mu\text{s})$ without sacrificing spectral resolution. The FFT is made on a full IGM that has a duration of 1/(99.7 Hz) which yields a frequency resolution of 99.7 Hz on a spectrum centered at several MHz.

## 5.2 RF to Optical Frequencies

To convert the RF spectrum back to optical frequencies, two operations are made on the frequency axis $\nu_{RF}$. One is a multiplication by the compression factor $m$ to retrieve relative optical frequencies, which represent a spectrum with the correct optical bandwidth. A shift $\nu_{shift}$ is then applied to relocate the spectrum at optical frequencies $\nu_{opt}$:

$$\nu_{opt} = m \cdot \nu_{RF} + \nu_{shift}. \tag{5.1}$$

In the ideal case where $f_{rep}$ is a harmonic of $\delta f_{rep}$ and $f_{ceo,M} = f_{ceo,S} = 0$, the shift is simply $\nu_{shift} = \Delta\nu_{max} \cdot \lfloor \nu_0 / \Delta\nu_{max} \rfloor$ when the integer division is even (and slightly different if odd). Since our DFC system is not $f_{ceo}$-tunable, the frequency shift must be found by a separate reference measurement and is acquired with a calibrated grating-based monochromator (Horiba iHR320). Its output as a function of the grating angle is measured with lock-in detection [66] using a lock-in amplifier (Zurich Instruments MFLI), an optical chopper and a photodiode. For this measurement, lock-in detection removes fluctuations in the recorded signal by relying on the reference signal provided by the optical chopper. To reproduce a spectrum that is comparable with the one measured with the DFC setup, the spectrum of the Master and Slave are separately sent in the monochromator and the squared root of the product of the spectra is computed. As in figure 4.2b, a multiplicative factor of $\lambda^2/c$ is applied to the spectrum measured with the monochromator when converting them from wavelengths to frequencies. The result of this procedure is shown in orange in figure 5.2 and compared to the shifted optical spectrum found with the DFC setup in blue.

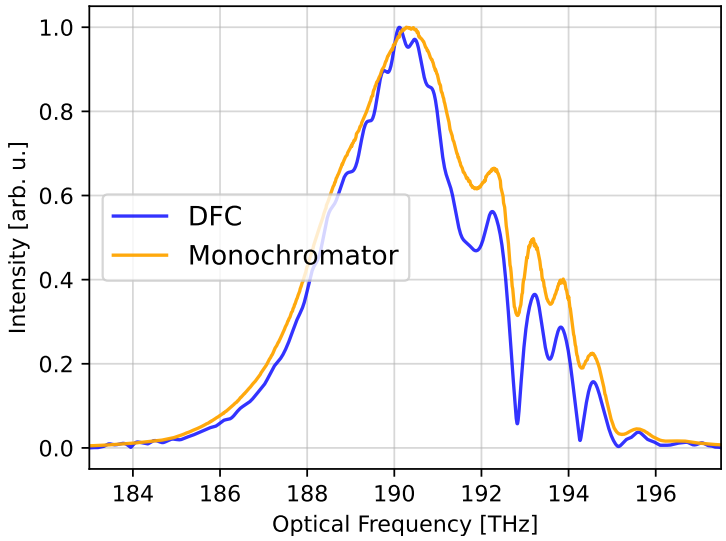


Figure 5.2 Optical spectrum of the un-broadened DFC source (blue) compared to a reference measurement made with a calibrated monochromator (orange). For the monochromator measurements, the grating step size corresponds to a wavelength shift of 1 nm, which yields a point spacing of ≈121 GHz at the central frequency. The DFC spectrum is shifted by 153.23 THz to match the features and general behaviour of the orange curve.

Figure 5.2 shows great agreement between both spectra after the one measured with the DFC setup is shifted by $\nu_{shift}$ =153.23 THz. This ideal shift is found via a numerical cross-correlation between the DFC spectrum resulting from the measurement with the monochromator and the RF spectrum from figure 5.1d after it is converted to relative optical frequencies. The ideal shift $\Delta\nu_{max} \cdot \lfloor \nu_0/\Delta\nu_{max} \rfloor$=150.47 THz is slightly off and the difference may be the result of either $|\Delta f_{ceo}| > \delta f_{rep}$ or the fact that $f_{rep}$ is not an exact harmonic of the detuning; both effects can shift the RF spectrum. Nevertheless, the spectrum in blue is much better resolved with respect to the reference measurement which has a point spacing of ≈121 GHz and to first order, can be seen as the resolution of the spectrum (since the width of the exit slit plays an important role in the resolution). The resolution (or point spacing) of the DFC spectrum can be found by multiplying the RF resolution with the compression factor and yields $f_{rep} + \delta f_{rep}$=99.999539 MHz according to equation 2.16. The resolution on the spectrum acquired with a single DFC IGM obtained in 10 ms is thus more than 3 orders of magnitude better than the one of the reference measurement. Concerning the intensity mismatch between both spectra on the higher frequency side, we attribute it to the width of the exit slit of the monochromator that is set too wide for the grating step size. This causes the nearby points on the spectrum to be slightly correlated and more intense than they actually are in a way to artificially reduce the resolution of the spectrum.

## 5.3 Coherent Averaging

To benefit from the periodic IGMs generated with a DFC interferometer, they must be coherently averaged to improve the SNR. Since our system is not stabilized against absolute references, the fluctuations of $f_{rep}$ and $\delta f_{rep}$ must be corrected for in post-processing. The correction algorithm used is inspired from [45, 67] and relies on the interpolation of the IGMs' CEP and arrival time. The fluctuating CEP is removed and the remaining signal is numerically resampled to counter the effects of the fluctuating repetition rate difference.

### 5.3.1 Correction of Fluctuations

To correct for the fluctuations of $\delta f_{rep}$ and $f_{ceo,RF}$, the time separation between the IGMs and their CEP are computed by first locating the maximum of the envelope of each IGM. The time separation is simply the time difference between two consecutive IGMs and the arrival time of the first (or zeroth) IGM applies a global time shift. The CEP is the phase of the real signal at the time corresponding to the maximum of the envelope. Comprised between $\pm\pi$, the CEPs are unwrapped by adding $k_i \cdot 2\pi$ to every $\text{CEP}_i$, where $k_i$ is an integer that ensures that the unwrapped CEPs are within $\pi$ of each other. Both of those quantities are sampled

only once per IGM and a cubic interpolation is made in between to enable correction of the drifts. Figure 5.3 shows the computed and interpolated arrival time of the IGMs and their unwrapped CEP.

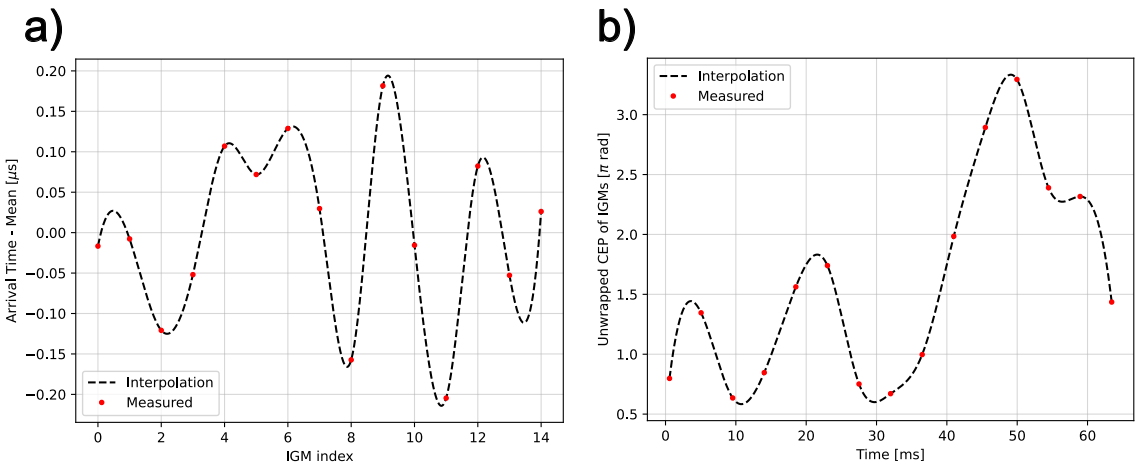


Figure 5.3 a) Measured (red dots) and interpolated (black, dashed) variation of the time separation between the IGMs for a mean separation of ≈ 4.5 ms ($\delta f_{rep}$=222 Hz). b) Measured (red dots) and interpolated (black, dashed) unwrapped CEP of the IGMs computed at their arrival time.

With figure 5.3a, we can witness once again the stability of the detuning between both combs from an IGM to another. Once the mean time separation of ≈ 4.5 ms is removed, the fluctuations of the detuning remain within ≈ ± 0.2 $\mu$s which represents a fractional stability better than 0.01 %. The correction of those drifts is still crucial to make sure the spectrum resulting from the sequential IGMs have the same bandwidth. With figure 5.3b, it's clear that the CEP is varying in time due to a combination of a non-zero $f_{ceo,RF}$ and its fluctuations. Since the nominal repetition rate is not necessarily a harmonic of the detuning, the fluctuations of the detuning may show up in the fluctuations of the unwrapped CEP. Independently of the cause of the fluctuations of the IGMs' CEP, they must be corrected to enable coherent averaging. If only the fluctuations of $\delta f_{rep}$ are corrected, two sequential IGMs with the same spectral information could potentially have a CEP$_i$=0 and the next one CEP$_{i+1} = \pi$ and *destructively interfere* when averaged. Any other combination of CEPs may produce an averaged IGM with washed-out features, hence why they must be interpolated and corrected to have the same CEP.

For the CEP drifts, the correction procedure is rather simple and consists of removing the interpolated CEP $\phi_{CEP,interp}$ from the analytical IGM sequence:

$$S_{BD}(t)_{CEP,cor} = S_{BD}(t) \cdot e^{-i\phi_{CEP,interp}(t)}, \tag{5.2}$$

where $S_{BD}(t)_{CEP,cor}$ is the CEP-corrected signal which contains a sequence of IGMs that all have a CEP=0. In the frequency domain, the RF spectrum may be slightly shifted after removing $\phi_{CEP,interp}$ since it's forcing $f_{ceo,RF}$ to zero. This is not a concern as the spectrum is appropriately shifted once converted to optical frequencies. In between the IGMs, the phase is modified according to the interpolation shown on figure 5.3b. The effect of this correction in the time domain is seen on figure 5.4, where the varying CEP in the left column is forced to zero via equation 5.2 on the right column.

To correct for the fluctuations of $\delta f_{rep}$ shown on figure 5.3a, the CEP-corrected signal in equation 5.2 is resampled based on the arrival-time interpolation. The resampling operation consists of another interpolation which compresses or stretches the signal in order to yield a constant time separation between the sequential IGMs; it also resolves the varying-bandwidth issue. On figure 5.4, the effect of the correction of the detuning shows up as zero-centered IGMs.

### 5.3.2 SNR Improvement

Once the fluctuations in the IGMs are corrected, they are ready to be coherently averaged in order to improve the SNR. However, the coherence time of the DFC system limits the number of IGMs that can be coherently averaged, even with appropriate corrections. It can be characterized by computing the cumulative SNR as a function of the number of IGMs that are averaged. The SNR is computed for the first IGM and the second one is added, where the SNR is computed on the resulting IGM; the procedure is repeated for all IGMs of the measurement. For a perfectly coherent DFC source, the SNR should grow proportionally to $\sqrt{N}$, where $N$ is the number of IGMs that are cumulatively averaged [4]. Figure 5.5 shows the cumulative SNR as a function of the measurement time for both the corrected and uncorrected IGMs for 99 sequential IGMs recorded with a detuning of 1.003 kHz.

With figure 5.5, we can see a clear improvement in the cumulative SNR when the corrections are applied to the IGMs, compared to the raw IGMs where the coherent averaging procedure rapidly degrades the SNR. In addition to the SNR, the central frequency, bandwidth and sharp features of the resulting spectrum are also modified when adding IGMs with significant fluctuations within them. When applying the correction procedure, these effects also show up, but after longer measurement times. Here, the SNR peaks at 1083 around 56 ms, but the content of the averaged IGM at this point is already starting to be deformed in a similar way than with the uncorrected IGMs. Up to $\approx$ 20 ms, the cumulative SNR dots in blue follow almost perfectly the ideal case proportional to the squared root of the number of IGMs, where the SNR of the first IGM is 187.3.

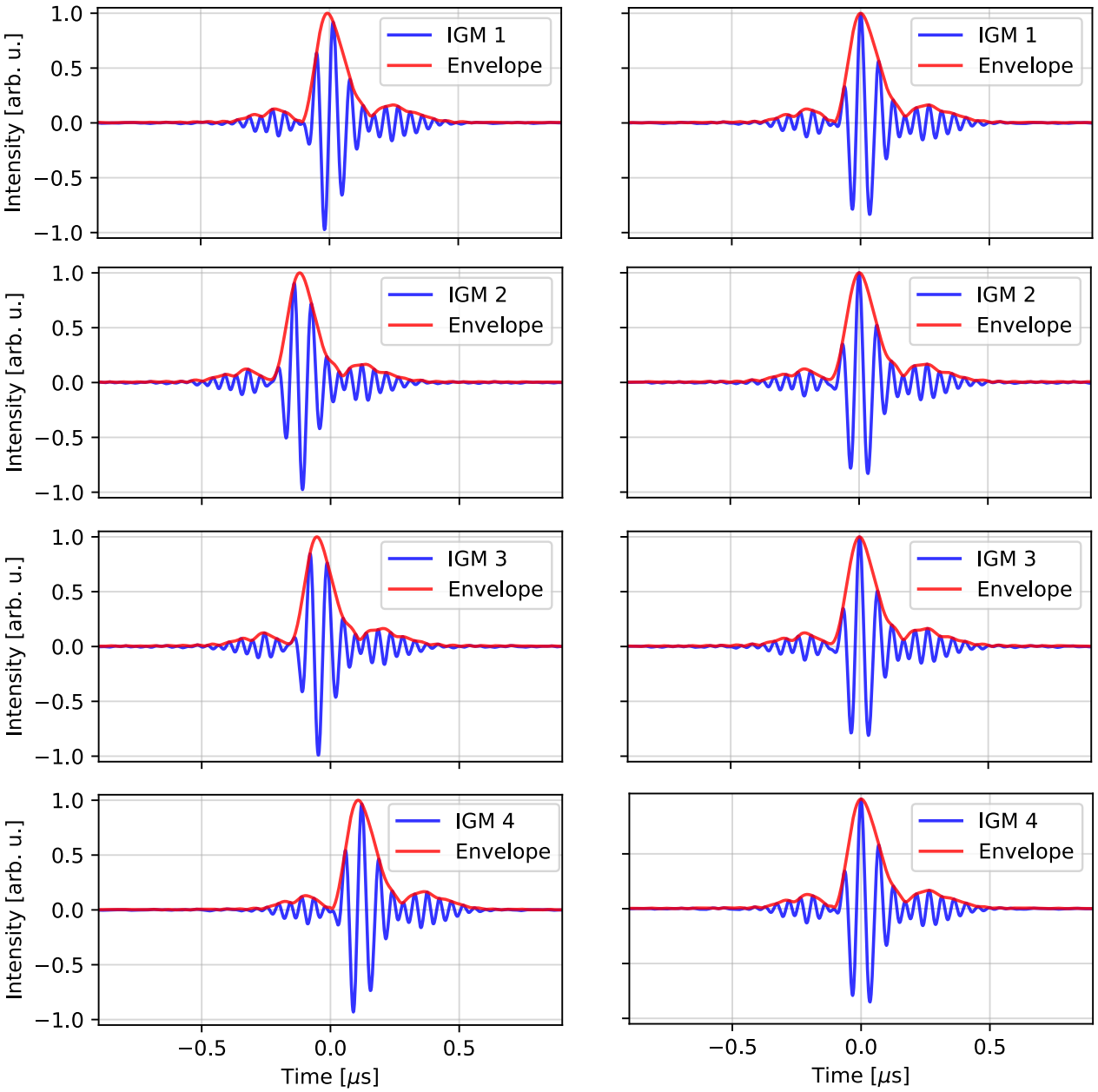


Figure 5.4 Left column: IGMs with indexes 1 to 4 from figure 5.3 before applying the corrections. The IGMs are offset by their arrival time difference minus the mean, which corresponds to $t = 0$ $\mu$s. Right column: same four IGMs after corrections.

The ADC used for the DFC measurements presented digitization and timing errors past 60 ms and may be the main cause for the decreasing cumulative SNR and short coherence time. It also prevented us from recording longer acquisitions, which may accumulate uncorrected low frequency noise and artificially degrade the SNR after only a couple of IGMs are averaged. After even longer acquisition times, it would have been seen that the coherence of the

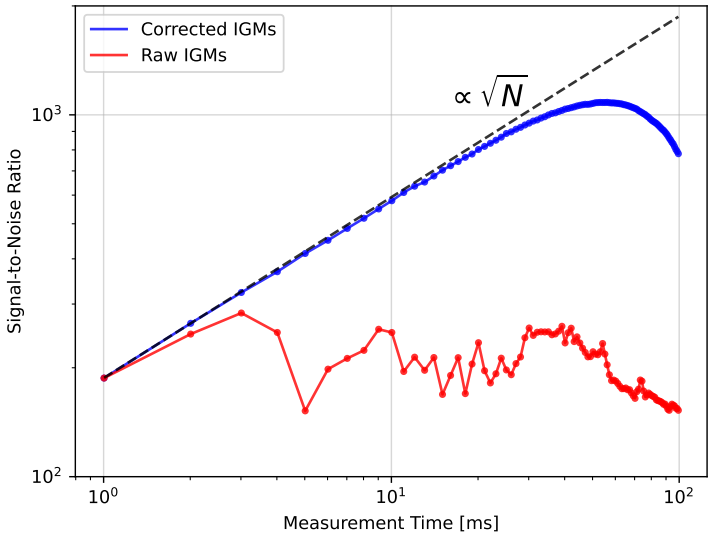


Figure 5.5 SNR as a function of the measurement time for the raw IGMs (red) and when the corrections on $f_{ceo,RF}$ and $\delta f_{rep}$ are applied (blue) for 99 IGMs acquired with a detuning of 1.003 kHz. Both axes are on a logarithmic scale and the ideal SNR scaling law proportional to $\sqrt{N}$, where $N$ is the number of averaged IGMs, is illustrated with a black dashed line.

DFC source would reach a comparable level than of the one found without correcting the fluctuations of both degrees of freedom of the measured RF comb, which would indicate after how much time both combs lose their mutual coherence.

## 5.4 Spectroscopy of Acetylene

The capabilities of our DFC system is demonstrated once again by measuring the absorption and dispersion of an acetylene sample around 196 THz. The gas is contained in a 5 cm fused silica cell with wedged interfaces (Thorlabs GCA50) to prevent etalon effects like the one observed in figure 5.1b and is placed in the path of the Slave comb as shown in figure 4.1. Since the Master does not see the analyte, the transmission in amplitude and dispersion of the sample is retrieved with equations 4.9 if a reference measurement without it is recorded.

Even if they were made for this purpose, the fibers discussed in section 4.4 are not used for this measurement because they yield lower optical powers and complicate the alignment; future measurements would, of course, benefit from their introduction in the setup. The un-broadened spectrum of both combs is therefore used where a small part of them overlaps with the low-frequency part (or P-branch) of the ro-vibrational spectrum of acetylene. Its bandwidth is about 2.5 THz wide, and a narrow band-pass filter centered at 1530 nm (Thor-

labs FBH1530-12) is used to keep only the relevant part of the spectrum. A detuning of 1.003 kHz is chosen to safely meet the Nyquist condition. Without the nonlinear broadening, it is almost impossible to be sensible to the rest of the absorption features past 197 THz (R-branch), but few enough peaks are expected and sufficient to characterize the behaviour of the DFC system. Figure 5.6a shows the inverted coherently averaged RF spectrum resulting from two sequential measurements of 60 IGMs: one reference measurement in blue and a second one in red with the sample in place.

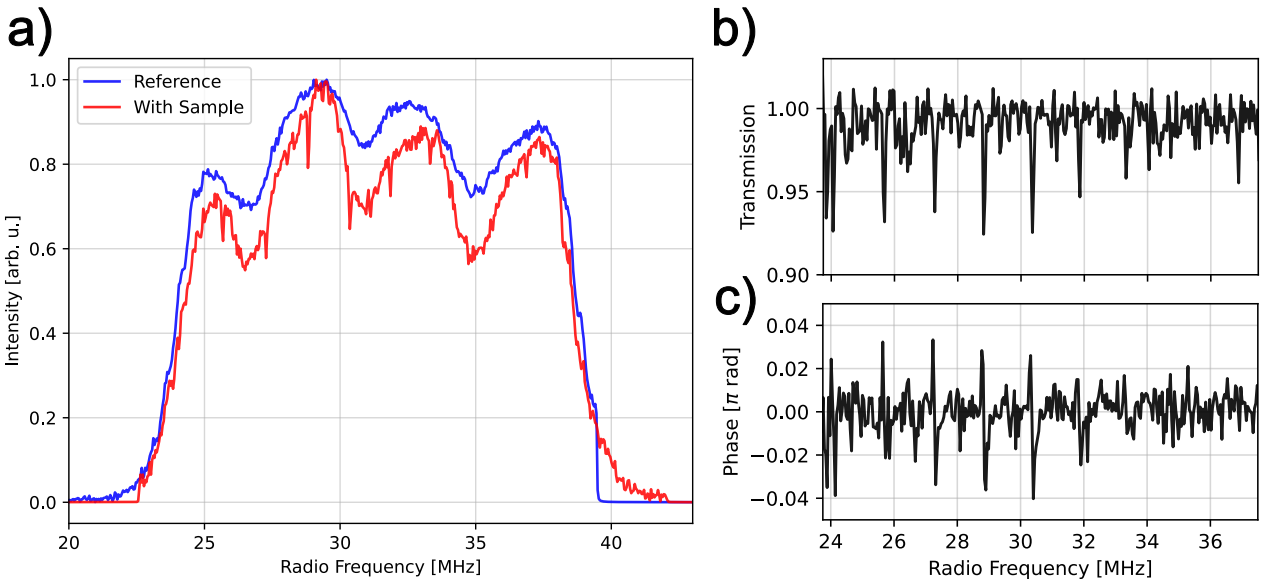


Figure 5.6 a) Normalized RF spectrum after inversion with respect to $f_{rep}/4$ with (red) and without (blue) the acetylene sample in the path of Slave comb for 60 coherently averaged IGMs acquired with a detuning of 1.003 kHz. b) RF transmission spectrum of acetylene after removing its slowly varying baseline. c) RF spectral phase of acetylene after removing its slowly varying baseline and shifting it to 0 rad.

A comparison between both spectra of figure 5.6a reveals a hand-full of absorption dips due to the presence of acetylene in the path of the Slave laser. Since they come from separate measurements and neither of the optical $f_{ceo}$s is stabilized, $\Delta f_{ceo}$ may drift and shift the spectrum between both measurements, which can be separated by a couple seconds or minutes. A cross-correlation between both RF spectra is made to realign both of them; the central frequency of the final RF spectra is not important here since the appropriate shift is applied once converting the spectrum to optical frequencies. The sharp drops in the transmitted spectrum (red line) at ≈23 MHz and in the reference one (blue line) at ≈39 MHz are the signature of an aggressive numerical filtering procedure and are not concerning since we focus on the absorption features in the central part of the spectrum. Even after normalizing both spectra, there seems to be notable absorption across the whole detection bandwidth, but it

can be attributed to reflections at the interfaces of the cell or downstream losses in the setup due to a slightly different optical path. Nevertheless, the transmission and phase information of the sample can be adequately retrieved from the spectra from figure 5.6 by applying a baseline-removal algorithm [68, 69]. Figures 5.6b and c show the measured transmission and spectral phase once the oscillating baseline is removed. Although they are not very prominent and there is a lot of noise, sharp absorption dips and phase jumps are revealed. The radio frequencies are converted to optical frequencies to compare the measured features with the ones reported in the HITRAN database [70]; the comparison is shown on figure 5.7.

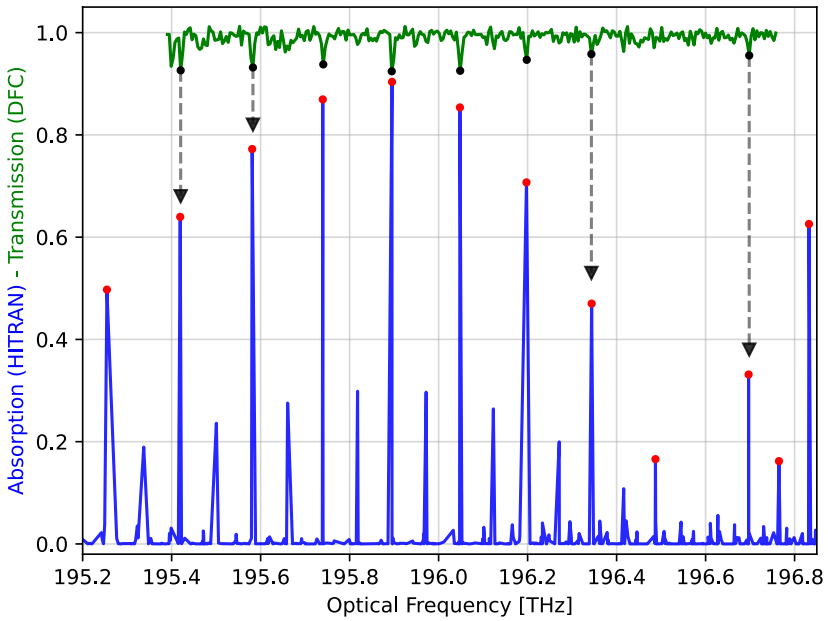


Figure 5.7 Absorption of acetylene around 196 THz from the HITRAN database measured with FTIR spectroscopy (blue) and transmission measured with the DFC setup after being shifted by 193.023 THz (green). The red dots indicate the most intense absorption peaks from the reference and are compared to the black dots that highlight the most resolved features from our transmission measurement.

For the acetylene measurement, no reference measurement is done with a spectrometer to determine the shift that must be applied to the relative optical frequencies. Instead, the absorption of acetylene from HITRAN is taken as an external reference and the shift is found by comparing the mode separation of the main features. For linear molecules like acetylene, the mode spacing is not exactly constant as a function of frequency [71] and this property is used to realign the measured transmission spectrum to the reference absorption spectrum. This can be seen as an approximate and manual cross-correlation that indicates to which transition each measured dip corresponds. Even with the transmission SNR barely greater than one, figure 5.7 still shows clear agreement between the frequencies of the transitions

after it's been rigidly shifted following this procedure. The remaining errors may be due to a slight error in the applied shift or the compression factor that applies a different shift to every transition. Another cause of error is that only the minimal point in the absorption dip is used instead of fitting the actual line-shape and then extract the central frequency of the transition. This additional step would only be beneficial with greater signal which can be done by increasing the effective sample length by modifying the setup to allow for multiple passes in the gas cell.

# CHAPTER 6 CONCLUSION

## 6.1 Summary of Works

The main goal of this project was to assemble, characterize and propose real-time correction protocols for a free-running DFC system with an actively controlled detuning of the repetition rates. Their spectrum and spectral phase were first characterized through SHG-FROG measurements, which revealed they are near transform-limited and well suited for $f$-$2f$ interferometry measurements to characterize their free-running $f_{ceo}$. These measurements showed slow drifts over several minutes, which is not concerning considering the length of our measurements. More importantly, the time stability of both repetition rates was characterized over a few hours and so was the stability of the detuning between both of them to ensure that the time separation between the sequential IGMs would be stable enough to envision coherent averaging. During the course of this project, the SHG-FROG setup, the PLL maintaining a fixed detuning between both combs and the optical setup producing periodic IGMs were assembled and characterized. Although they were not used for their main purpose, home-made HNF assemblies were designed to enable broadband spectroscopy.

The optical DFC setup successfully produced periodic IGMs under various configurations and the optical spectrum of the unbroadened source was adequately retrieved by comparing it to a measurement made with a calibrated monochromator. The fluctuations in the CEP phase and arrival time of the individual IGMs is numerically corrected through interpolation and resampling of the IGM train to yield a coherently averaged IGM with a cumulative SNR following the ideal $\sqrt{N}$ scaling law for a couple tens of milliseconds. The final characterization step of the DFC interferometer is to show its capability to retrieve the absorption and spectral phase of an acetylene sample placed in a dispersive configuration. Only being preliminary results, promising agreement between our measurement and the HITRAN database is shown within the SNR attained in the experiment.

## 6.2 Limitations

The Master laser unexpectedly broke down twice in less than a year and required oversea repairs both times, which made the PLL and DFC setup simply unusable for more than six months. These failures prevented us from measuring more convincing acetylene absorption with the HNF assemblies. The ADC used for most measurements presented strange and unpredictable sampling behaviour past ≈100 ms and limited the depth of the

analysis of the coherence time of the DFC setup. Moreover, the file size involved in our DFC measurements often reached 250 to 500 MB on which many FFTs and interpolations are performed and made the analysis very computationally demanding. In absolutely referenced DFC setups, real-time coherent averaging is possible in a way to reduce the effective file size [33], but this method is hardly applicable here since the averaging procedure first needs a post-measurement correction of the IGMs.

### 6.3 Future Research

To improve the SNR and reduce the noise in our DFC experimental setup, both combs could be split in three parts: one part for the spectroscopic measurement, another to monitor the repetition rate and one for $f_{ceo}$. Each comb would require its own frequency counter for the repetition rate and $f$-to-$2f$ interferometer for $f_{ceo}$. Additionally, these four measurements must be registered on separate channels of an ADC and sampled at the same rate as the main experiment (or faster). This method would improve the coherent averaging procedure by no longer relying on average values of the nominal repetition rate and detuning. A real-time measurement of $f_{ceo}$ of each comb would also improve the CEP removal and enable real-time characterization of $f_{ceo,RF}$. This modified system would be much more robust against environmental fluctuations and would still only rely on a post-processing correction algorithm instead of a complex and fully referenced DFC system. Alternatively, the DFC system would benefit from an $f_{ceo}$-free RF comb where CEP fluctuations are cancelled out by the DFG process [37].

To follow up with the characterization steps presented in this thesis, the setup may be improved to make precise, fast and broadband characterization (absorption, dispersion or both) of samples or fibers by adding a $4f$-shaper to act as a tunable spatial frequency filter [72]. As mentioned in section 5.4 in the case of gaseous samples, the setup may be modified to enable multiple passes to increase its effective length and improve the SNR. Combined with the broadband output of the HNFs in chapter 4.4, these additions would be ideal for broadband and sensitive characterization and removes the need for traditional optical filters.

Another interesting direction to explore would be to convert the DFC system to the MIR via DFG. For a single frequency comb, this has been done previously in our laboratory [73] by broadening the spectrum with SCG and combining a part of it with the fundamental spectrum in a Periodically Poled Lithium Niobate (PPLN) crystal to yield phase-stable MIR pulses. To apply this method to our DFC setup, both combs would require to be converted in the MIR following this procedure and then be interfered to generate periodic IGMs. Again, DFG would provide $f_{ceo}$-free combs, dramatically simplifying error-correction procedures.

# REFERENCES


[1] N. Picqué and T. W. Hänsch, "Frequency comb spectroscopy," *Nature Photonics*, vol. 13, no. 3, pp. 146–157, Mar. 2019, number: 3 Publisher: Nature Publishing Group. [Online]. Available: https://www.nature.com/articles/s41566-018-0347-5

[2] L. A. Sterczewski, J. Westberg, and G. Wysocki, "Computational coherent averaging for free-running dual-comb spectroscopy," *Optics Express*, vol. 27, no. 17, pp. 23 875–23 893, Aug. 2019, publisher: Optica Publishing Group. [Online]. Available: https://opg.optica.org/oe/abstract.cfm?uri=oe-27-17-23875

[3] S. Schilt and T. Südmeyer, "Carrier-Envelope Offset Stabilized Ultrafast Diode-Pumped Solid-State Lasers," *Applied Sciences*, vol. 5, no. 4, pp. 787–816, Dec. 2015, number: 4 Publisher: Multidisciplinary Digital Publishing Institute. [Online]. Available: https://www.mdpi.com/2076-3417/5/4/787

[4] I. Coddington, N. Newbury, and W. Swann, "Dual-comb spectroscopy," *Optica*, vol. 3, no. 4, pp. 414–426, Apr. 2016, publisher: Optica Publishing Group. [Online]. Available: https://opg.optica.org/optica/abstract.cfm?uri=optica-3-4-414

[5] "Converting between $F_{\nu}$ and $F_{\lambda}$ spectral density," Sep. 2022. [Online]. Available: https://physics.stackexchange.com/q/725928

[6] S. Chu, J. O. Stoner, G. S. Hurst, and J. D. Graybeal, "Spectroscopy," Sep. 2023. [Online]. Available: https://www.britannica.com/science/spectroscopy

[7] Steve Buckley, "Detecting Methane Emissions: How Spectroscopy is Contributing to Sustainability Efforts," *Spectroscopy*, vol. 37, no. 4, pp. 22–26, Apr. 2022. [Online]. Available: https://www.spectroscopyonline.com/view/detecting-methane-emissions-how-spectroscopy-is-contributing-to-sustainability-efforts

[8] "Greenhouse Gas and Atmospheric Trace Gas Measurements," *NIST*. [Online]. Available: https://www.nist.gov/programs-projects/greenhouse-gas-and-atmospheric-trace-gas-measurements

[9] Q. Liang, Y.-C. Chan, J. Toscano, K. K. Bjorkman, L. A. Leinwand, R. Parker, E. S. Nozik, D. J. Nesbitt, and J. Ye, "Breath analysis by ultra-sensitive broadband laser spectroscopy detects SARS-CoV-2 infection," *J. Breath Res.*, vol. 17, no. 3, p. 036001, Apr. 2023. [Online]. Available: https://dx.doi.org/10.1088/1752-7163/acc6e4

[10] D.-W. Sun, Ed., *Infrared Spectroscopy for Food Quality Analysis and Control*. San Diego: Academic Press, Jan. 2009. [Online]. Available: https://www.sciencedirect.com/science/article/pii/B9780123741363000201

[11] A. Biancolillo and F. Marini, "Chemometric Methods for Spectroscopy-Based Pharmaceutical Analysis," *Frontiers in Chemistry*, vol. 6, 2018. [Online]. Available: https://www.frontiersin.org/articles/10.3389/fchem.2018.00576

[12] N. Picqué and T. W. Hänsch, "Mid-IR Spectroscopic Sensing," *Optics and Photonics News Magazine*, Jun. 2019. [Online]. Available: https://www.optica-opn.org/home/articles/volume_30/june_2019/features/mid-ir_spectroscopic_sensing/

[13] A. A. Michelson and E. W. Morley, "On the relative motion of the Earth and the luminiferous ether," *American Journal of Science*, vol. s3-34, no. 203, pp. 333–345, Nov. 1887, publisher: American Journal of Science. [Online]. Available: https://ajsonline.org/article/62505

[14] R. Loudon, *The Quantum Theory of Light*, third edition, third edition ed. Oxford, New York: Oxford University Press, Nov. 2000.

[15] A. Dutt, C. Joshi, X. Ji, J. Cardenas, Y. Okawachi, K. Luke, A. L. Gaeta, and M. Lipson, "On-chip dual-comb source for spectroscopy," *Science Advances*, vol. 4, no. 3, p. e1701858, Mar. 2018, publisher: American Association for the Advancement of Science. [Online]. Available: https://www.science.org/doi/10.1126/sciadv.1701858

[16] B. E. A. Saleh and M. C. Teich, *Fundamentals of Photonics*, 2nd ed. Wiley, 2007.

[17] R. Paschotta, "Kerr Effect," Feb. 2008. [Online]. Available: https://www.rp-photonics.com/kerr_effect.html

[18] T. Brabec, C. Spielmann, P. F. Curley, and F. Krausz, "Kerr lens mode locking," *Optics Letters*, vol. 17, no. 18, pp. 1292–1294, Sep. 1992, publisher: Optica Publishing Group. [Online]. Available: https://opg.optica.org/ol/abstract.cfm?uri=ol-17-18-1292

[19] M. Piché and F. Salin, "Self-mode locking of solid-state lasers without apertures," *Optics Letters*, vol. 18, no. 13, pp. 1041–1043, Jul. 1993, publisher: Optica Publishing Group. [Online]. Available: https://opg.optica.org/ol/abstract.cfm?uri=ol-18-13-1041

[20] D. R. Paschotta, "Time-Bandwidth Product." [Online]. Available: https://www.rp-photonics.com/time_bandwidth_product.html

[21] D. Kane and R. Trebino, "Characterization of arbitrary femtosecond pulses using frequency-resolved optical gating," *IEEE Journal of Quantum Electronics*, vol. 29, no. 2, pp. 571–579, Feb. 1993, conference Name: IEEE Journal of Quantum Electronics. [Online]. Available: https://ieeexplore.ieee.org/document/199311

[22] A. M. Weiner, *Ultrafast Photonics*, ser. Wiley series in pure and applied optics. Wiley, 2009.

[23] R. Paschotta, A. Schlatter, S. Zeller, H. Telle, and U. Keller, "Optical phase noise and carrier-envelope offset noise of mode-locked lasers," *Applied Physics B*, vol. 82, no. 2, pp. 265–273, Feb. 2006. [Online]. Available: https://doi.org/10.1007/s00340-005-2041-9

[24] R. Paschotta, "Carrier-envelope offset," Nov. 2007. [Online]. Available: https://www.rp-photonics.com/carrier_envelope_offset.html

[25] H. Telle, G. Steinmeyer, A. Dunlop, J. Stenger, D. Sutter, and U. Keller, "Carrier-envelope offset phase control: A novel concept for absolute optical frequency measurement and ultrashort pulse generation," *Applied Physics B*, vol. 69, no. 4, pp. 327–332, Oct. 1999. [Online]. Available: https://doi.org/10.1007/s003400050813

[26] J. Rauschenberger, T. M. Fortier, D. J. Jones, J. Ye, and S. T. Cundiff, "Control of the frequency comb from a mode-locked Erbium-doped fiber laser," *Optics Express*, vol. 10, no. 24, pp. 1404–1410, Dec. 2002, publisher: Optica Publishing Group. [Online]. Available: https://opg.optica.org/oe/abstract.cfm?uri=oe-10-24-1404

[27] T. W. Hänsch, "Nobel Lecture: Passion for precision," *Reviews of Modern Physics*, vol. 78, no. 4, pp. 1297–1309, Nov. 2006. [Online]. Available: https://link.aps.org/doi/10.1103/RevModPhys.78.1297

[28] S. A. Diddams, "The evolving optical frequency comb [Invited]," *Journal of the Optical Society of America B*, vol. 27, no. 11, p. B51, Nov. 2010. [Online]. Available: https://opg.optica.org/abstract.cfm?URI=josab-27-11-B51

[29] J. A. Boyd and T. Lahaye, "A basic introduction to ultrastable optical cavities for laser stabilization," *American Journal of Physics*, vol. 92, no. 1, pp. 50–58, Jan. 2024. [Online]. Available: https://doi.org/10.1119/5.0161369

[30] R. Paschotta, "Noise in Laser Technology," *Optik & Photonik*, vol. 4, no. 2, pp. 48–50, 2009, _eprint: https://onlinelibrary.wiley.com/doi/pdf/10.1002/opph.201190028. [Online]. Available: https://onlinelibrary.wiley.com/doi/abs/10.1002/opph.201190028

[31] N. Torcheboeuf, G. Buchs, S. Kundermann, E. Portuondo-Campa, J. Bennès, and S. Lecomte, "Repetition rate stabilization of an optical frequency comb based on solid-state laser technology with an intra-cavity electro-optic modulator," *Optics Express*, vol. 25, no. 3, pp. 2215–2220, Feb. 2017, publisher: Optica Publishing Group. [Online]. Available: https://opg.optica.org/oe/abstract.cfm?uri=oe-25-3-2215

[32] T. Yu, S. Jiang, J. Fang, T. Liu, X. Wu, M. Yan, K. Huang, and H. Zeng, "Passive repetition-rate stabilization for a mode-locked fiber laser by electro-optic modulation," *Optics Letters*, vol. 47, no. 5, pp. 1178–1181, Mar. 2022, publisher: Optica Publishing Group. [Online]. Available: https://opg.optica.org/ol/abstract.cfm?uri=ol-47-5-1178

[33] I. Coddington, W. C. Swann, and N. R. Newbury, "Coherent dual-comb spectroscopy at high signal-to-noise ratio," *Physical Review A*, vol. 82, no. 4, p. 043817, Oct. 2010, publisher: American Physical Society. [Online]. Available: https://link.aps.org/doi/10.1103/PhysRevA.82.043817

[34] L.-S. Ma, M. Zucco, S. Picard, L. Robertsson, and R. Windeler, "A new method to determine the absolute mode number of a mode-locked femtosecond-laser comb used for absolute optical frequency measurements," *IEEE Journal of Selected Topics in Quantum Electronics*, vol. 9, no. 4, pp. 1066–1071, Jul. 2003, conference Name: IEEE Journal of Selected Topics in Quantum Electronics. [Online]. Available: https://ieeexplore.ieee.org/document/1250463

[35] Z. Wei, H. Han, W. Zhang, Y. Zhao, J. Zhu, H. Teng, Q. Du, Z. Wei, H. Han, W. Zhang, Y. Zhao, J. Zhu, H. Teng, and Q. Du, "Measurement and Control of Carrier-Envelope Phase in Femtosecond Ti:sapphire Laser," in *Advances in Solid State Lasers Development and Applications*. IntechOpen, Feb. 2010. [Online]. Available: https://www.intechopen.com/chapters/8413

[36] G. Ycas, F. R. Giorgetta, E. Baumann, I. Coddington, D. Herman, S. A. Diddams, and N. R. Newbury, "High-coherence mid-infrared dual-comb spectroscopy spanning 2.6 to 5.2 m," *Nature Photonics*, vol. 12, no. 4, pp. 202–208, Apr. 2018, number: 4 Publisher: Nature Publishing Group. [Online]. Available: https://www.nature.com/articles/s41566-018-0114-7

[37] D. Fehrenbacher, P. Sulzer, A. Liehl, T. Kälberer, C. Riek, D. V. Seletskiy, and A. Leitenstorfer, "Free-running performance and full control of a passively phase-stable Er:fiber frequency comb," *Optica*, vol. 2, no. 10, pp. 917–923,

Oct. 2015, publisher: Optica Publishing Group. [Online]. Available: https://opg.optica.org/optica/abstract.cfm?uri=optica-2-10-917

[38] A. Baltuška, T. Fuji, and T. Kobayashi, "Controlling the Carrier-Envelope Phase of Ultrashort Light Pulses with Optical Parametric Amplifiers," *Physical Review Letters*, vol. 88, no. 13, p. 133901, Mar. 2002. [Online]. Available: https://link.aps.org/doi/10.1103/PhysRevLett.88.133901

[39] S. A. Diddams, L. Hollberg, and V. Mbele, "Molecular fingerprinting with the resolved modes of a femtosecond laser frequency comb," *Nature*, vol. 445, no. 7128, pp. 627–630, Feb. 2007, number: 7128 Publisher: Nature Publishing Group. [Online]. Available: https://www.nature.com/articles/nature05524

[40] C. Gohle, B. Stein, A. Schliesser, T. Udem, and T. W. Hänsch, "Frequency Comb Vernier Spectroscopy for Broadband, High-Resolution, High-Sensitivity Absorption and Dispersion Spectra," *Physical Review Letters*, vol. 99, no. 26, p. 263902, Dec. 2007. [Online]. Available: https://link.aps.org/doi/10.1103/PhysRevLett.99.263902

[41] G. B. Lebron and T. L. Tan, "High-resolution FTIR measurement and analysis of the 3 band of C2H3D," *Journal of Molecular Spectroscopy*, vol. 261, no. 2, pp. 119–123, Jun. 2010. [Online]. Available: https://www.sciencedirect.com/science/article/pii/S0022285210000792

[42] S. Albert, S. Bauerecker, E. S. Bekhtereva, I. B. Bolotova, H. Hollenstein, M. Quack, and O. N. Ulenikov, "High resolution FTIR spectroscopy of fluoroform 12CHF3 and critical analysis of the infrared spectrum from 25 to 1500 cm1," *Molecular Physics*, vol. 116, no. 9, pp. 1091–1107, May 2018, publisher: Taylor & Francis _eprint: https://doi.org/10.1080/00268976.2017.1392628. [Online]. Available: https://doi.org/10.1080/00268976.2017.1392628

[43] C. R. Phillips, B. Willenberg, A. Nussbaum-Lapping, F. Callegari, S. L. Camenzind, J. Pupeikis, and U. Keller, "Coherently averaged dual-comb spectroscopy with a low-noise and high-power free-running gigahertz dual-comb laser," *Optics Express*, vol. 31, no. 5, pp. 7103–7119, Feb. 2023, publisher: Optica Publishing Group. [Online]. Available: https://opg.optica.org/oe/abstract.cfm?uri=oe-31-5-7103

[44] J.-D. Deschênes, P. Giaccarri, and J. Genest, "Optical referencing technique with CW lasers as intermediate oscillators for continuous full delay range frequency comb interferometry," *Optics Express*, vol. 18, no. 22, p. 23358, Oct. 2010. [Online]. Available: https://opg.optica.org/oe/abstract.cfm?uri=oe-18-22-23358

[45] N. Bourbeau Hébert and Université Laval. Faculté des sciences et de génie., "High-coherence dual-comb interferometry with free-running lasers," PhD Thesis, Université Laval, Québec, 2019. [Online]. Available: http://hdl.handle.net/20.500.11794/36903

[46] T. J. Parker, "Dispersive Fourier transform spectroscopy," *Contemporary Physics*, vol. 31, no. 5, pp. 335–353, Sep. 1990. [Online]. Available: https://doi.org/10.1080/00107519008213783

[47] S. Yan, M. T. Seidel, and H.-S. Tan, "Perturbed free induction decay in ultrafast mid-IR pump–probe spectroscopy," *Chemical Physics Letters*, vol. 517, no. 1-3, pp. 36–40, Nov. 2011. [Online]. Available: https://linkinghub.elsevier.com/retrieve/pii/S0009261411012656

[48] E. W. Weisstein, "Cross-Correlation." [Online]. Available: https://mathworld.wolfram.com/Cross-Correlation.html

[49] S. Vasilyev, A. Muraviev, D. Konnov, M. Mirov, V. Smolski, I. Moskalev, S. Mirov, and K. Vodopyanov, "Longwave infrared (6.6–11.4 µm) dual-comb spectroscopy with 240,000 comb-mode-resolved data points at video rate," *Opt. Lett., OL*, vol. 48, no. 9, pp. 2273–2276, May 2023. [Online]. Available: https://opg.optica.org/ol/abstract.cfm?uri=ol-48-9-2273

[50] F. Keilmann, C. Gohle, and R. Holzwarth, "Time-domain mid-infrared frequency-comb spectrometer," *Optics Letters*, vol. 29, no. 13, pp. 1542–1544, Jul. 2004, publisher: Optica Publishing Group. [Online]. Available: https://opg.optica.org/ol/abstract.cfm?uri=ol-29-13-1542

[51] A. Schliesser, M. Brehm, F. Keilmann, and D. W. v. d. Weide, "Frequency-comb infrared spectrometer for rapid, remote chemical sensing," *Optics Express*, vol. 13, no. 22, pp. 9029–9038, Oct. 2005, publisher: Optica Publishing Group. [Online]. Available: https://opg.optica.org/oe/abstract.cfm?uri=oe-13-22-9029

[52] N. B. Hébert, J. Genest, J.-D. Deschênes, H. Bergeron, G. Y. Chen, C. Khurmi, and D. G. Lancaster, "Self-corrected chip-based dual-comb spectrometer," *Optics Express*, vol. 25, no. 7, pp. 8168–8179, Apr. 2017, publisher: Optica Publishing Group. [Online]. Available: https://opg.optica.org/oe/abstract.cfm?uri=oe-25-7-8168

[53] D. Harvey, "Improving the Signal-to-Noise Ratio," Jan. 2021. [Online]. Available: https://chem.libretexts.org/Bookshelves/Analytical_Chemistry/Chemometrics_Using_R_(Harvey)/10%3A_Cleaning_Up_Data/10.2%3A_Signal_Averaging

[54] N. C. Geib, M. Zilk, T. Pertsch, and F. Eilenberger, "Common pulse retrieval algorithm: a fast and universal method to retrieve ultrashort pulses," *Optica*, vol. 6, no. 4, pp. 495–505, Apr. 2019, publisher: Optica Publishing Group. [Online]. Available: https://opg.optica.org/optica/abstract.cfm?uri=optica-6-4-495

[55] "2D Apodization/Weighting Function." [Online]. Available: https://web.stanford.edu/group/chem-NMR/help_docs/2dapodization.htm

[56] L. P. Ramirez, D. N. Papadopoulos, A. Pellegrina, P. Georges, F. Druon, P. Monot, A. Ricci, A. Jullien, X. Chen, J. P. Rousseau, and R. Lopez-Martens, "Efficient cross polarized wave generation for compact, energy-scalable, ultrashort laser sources," *Optics Express*, vol. 19, no. 1, p. 93, Jan. 2011. [Online]. Available: https://opg.optica.org/oe/abstract.cfm?uri=oe-19-1-93

[57] "Ultra-low-noise frequency comb offset stabilization." [Online]. Available: https://www.octavephotonics.com/resources/application-note-ultra-low-noise-frequency-comb-offset-stabilization

[58] "pyNLO: Nonlinear optics modeling for Python." [Online]. Available: https://pynlo.readthedocs.io/en/latest/

[59] D. R. Paschotta, "Effective Nonlinear Coefficient," Aug. 2016. [Online]. Available: https://www.rp-photonics.com/effective_nonlinear_coefficient.html

[60] "Highly Nonlinear Fiber with Anomalous Dispersion," Thorlabs, Tech. Rep., Mar. 2021. [Online]. Available: https://www.thorlabs.com/drawings/c687990c91736c08-9F8ED3A5-AC04-31BD-F5E502E71B935CAC/HN1550P-SpecSheet.pdf

[61] J. Hult, "A Fourth-Order Runge–Kutta in the Interaction Picture Method for Simulating Supercontinuum Generation in Optical Fibers," *Journal of Lightwave Technology*, vol. 25, no. 12, pp. 3770–3775, Dec. 2007, publisher: IEEE. [Online]. Available: https://opg.optica.org/jlt/abstract.cfm?uri=jlt-25-12-3770

[62] "scipy.signal.hilbert — SciPy v1.12.0 Manual." [Online]. Available: https://docs.scipy.org/doc/scipy/reference/generated/scipy.signal.hilbert.html

[63] D. R. Paschotta, "Etalons," Nov. 2006. [Online]. Available: https://www.rp-photonics.com/etalons.html

[64] "SCHOTT Optical Glass Data Sheets." [Online]. Available: https://refractiveindex.info/download/data/2017/schott_2017-01-20.pdf

[65] I. H. Malitson, "Interspecimen Comparison of the Refractive Index of Fused Silica*,†," *JOSA*, vol. 55, no. 10, pp. 1205–1209, Oct. 1965, publisher: Optica Publishing Group. [Online]. Available: https://opg.optica.org/josa/abstract.cfm?uri=josa-55-10-1205

[66] "Principles of Lock-in Detection | Zurich Instruments," Dec. 2019. [Online]. Available: https://www.zhinst.com/en/resources/principles-of-lock-in-detection

[67] N. B. Hébert, "selfCorrectIGMs." [Online]. Available: https://www.mathworks.com/matlabcentral/fileexchange/69759-selfcorrectigms

[68] X. Shen, S. Ye, L. Xu, R. Hu, L. Jin, H. Xu, J. Liu, and W. Liu, "Study on baseline correction methods for the Fourier transform infrared spectra with different signal-to-noise ratios," *Appl. Opt., AO*, vol. 57, no. 20, pp. 5794–5799, Jul. 2018. [Online]. Available: https://opg.optica.org/ao/abstract.cfm?uri=ao-57-20-5794

[69] P. H. C. Eilers and H. F. M. Boelens, "Baseline Correction with Asymmetric Least Squares Smoothing," *Unpubl. Manuscr*, Nov. 2005.

[70] L. S. Rothman, D. Jacquemart, A. Barbe, D. C. Benner, M. Birk, L. R. Brown, M. R. Carleer, C. Chackerian, K. Chance, L. H. Coudert, V. Dana, V. M. Devi, J.-M. Flaud, R. R. Gamache, A. Goldman, J.-M. Hartmann, K. W. Jucks, A. G. Maki, J.-Y. Mandin, S. T. Massie, J. Orphal, A. Perrin, C. P. Rinsland, M. A. H. Smith, J. Tennyson, R. N. Tolchenov, R. A. Toth, J. V. Auwera, P. Varanasi, and G. Wagner, "The HITRAN 2004 molecular spectroscopic database," *Journal of Quantitative Spectroscopy and Radiative Transfer*, vol. 96, no. 2, pp. 139–204, 2005. [Online]. Available: https://www.sciencedirect.com/science/article/pii/S0022407305001081

[71] J. M. Hollas, *Modern Spectroscopy.* John Wiley & Sons, Apr. 2004, google-Books-ID: lVyXQZkcKKkC.

[72] D. R. Paschotta, "Pulse Shapers," Jul. 2019. [Online]. Available: https://www.rp-photonics.com/pulse_shapers.html

[73] L. Rivard, "Development of a Versatile 76 MHz Fiber Based Source of 9-fs Pulses in the Near-Infrared and Phase-Stable ps Pulses in the Mid-Infrared," Master's thesis, Polytechnique Montréal, Jun. 2023. [Online]. Available: https://publications.polymtl.ca/54125/

# APPENDIX A SHG-FROG MEASUREMENT AND ANALYSIS OF SLAVE LASER

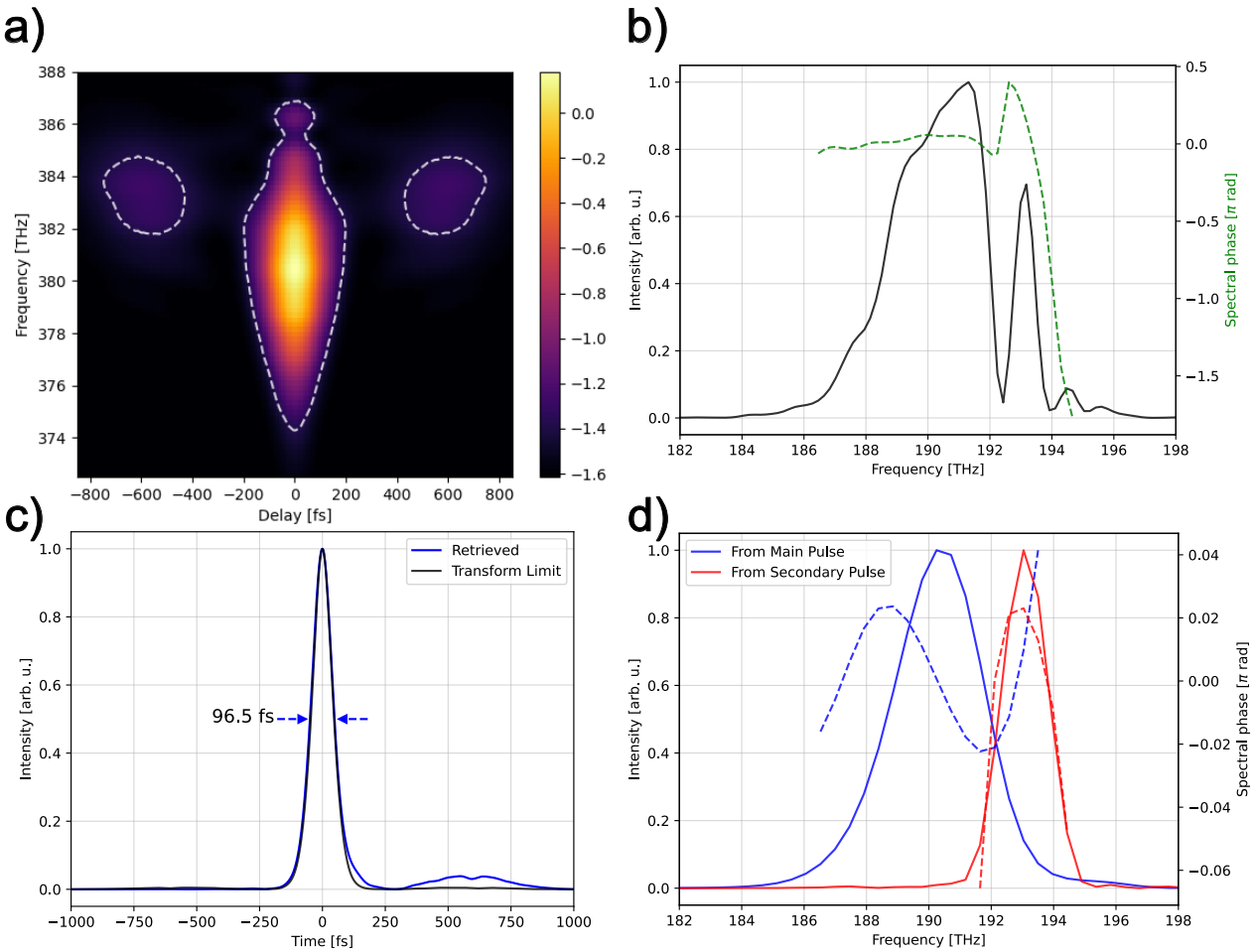


Figure A.1 a) SHG-FROG trace of the Slave laser with a spectrometer integration time of 85 ms where 10 points per delay were acquired. The intensity is plotted on a logarithmic scale and dashed contour lines reveal dimer features. The spectrogram was sampled for delays separated by $2\mu m/c$ covering a total range of $\pm$ 400 $\mu m/c$. b) Retrieved spectrum (black, full) and spectral phase (green, dashed) of Slave laser. c) Retrieved pulse with FWHM of 96.5 fs (blue) compared to its FTL (black). d) Spectra (full) and spectral phases (dashed) of the main retrieved pulse (blue) and secondary pulse (red). Both spectra are normalized to unity. A numerical time-domain filter was applied isolate both pulses and the $\approx$ 600 fs time separation between them matches the $\approx$ 1.6 THz interference fringes in the spectrum of b). The spectral phase of the main pulse is well within $\pm 0.05\pi$ and it is slightly quadratic for the secondary pulse.